Accuracy and Computational Cost Assessment of Radiation Solvers for Combustion Simulations

Chloe David
Marquette University

ACCURACY AND COMPUTATIONAL COST ASSESSMENT OF RADIATION SOLVERS FOR COMBUSTION SIMULATIONS

by

Chloe S. David, B.S.

A Thesis submitted to the Faculty of the Graduate School,
Marquette University,
in Partial Fulfillment of the Requirements for
the Degree of Master of Science

Milwaukee, Wisconsin

May 2021

ABSTRACT
ACCURACY AND COMPUTATIONAL COST
ASSESSMENT OF RADIATION
SOLVERS FOR COMBUSTION
SIMULATIONS

Chloe S. David, B.S.

Marquette University, 2021

High-fidelity combustion simulations necessitate the accurate and efficient calculation of radiative heat transfer. A successful radiation calculation requires the use of a spectral model, which describes the variation of radiative properties across the entire electromagnetic spectrum, and a radiative transfer equation (RTE) solver, which solves the governing equation for radiation transport. Three primary categories of RTE solvers are the discrete ordinates method (DOM), the spherical harmonics method (SHM), and the photon Monte Carlo (PMC) method. The accuracy and computational cost of each type of RTE solver is compared in detail in this work. The PMC RTE solver is considered the most accurate and rightly handles irregular geometries and highly nonhomogenous participating media. A deeper analysis of the computational load distribution of the PMC solver is conducted. Relations between the global computational load for PMC and local variables like temperature, Planck mean absorption coefficient, and cell volume are investigated.

ACKNOWLEDGMENTS

Chloe S. David, B.S.

I would first like to sincerely thank my thesis advisor, Dr. Somesh Roy, for his feedback and support throughout my Masters degree and research. I would not be where I am today without his valuable advice, patience, and encouragement to do the best work that I can. I would also like to thank my committee members, Dr. Simcha Singer and Dr. John Moore, for their time and feedback given to my thesis. Finally, I'd like to extend my gratitude to my family and friends for their continuous support of my success.

This research is supported by the National Science Foundation through Grant #1756005.

DEDICATION

I'd like to dedicate this work to the Lord. May Him be the glory forever and ever!

TABLE OF CONTENTS

LIST OF TABLES

LIST OF FIGURES

CHAPTER 1

INTRODUCTION

1.1 Motivation

The investigation of computational cost and accuracy in radiation solvers is important for two primary reasons. First, radiative heat transfer is a necessary component of accurate combustion modeling, especially in turbulent combustion. In other words, the results of combustion simulations that consider the radiation effect better match experimental data. Thus, high-fidelity combustion simulations necessitate accurate radiation calculations.

Second, radiation is a challenging mathematical and computational problem. Since radiation is particularly difficult to model, various numerical methods have been proposed to approximate the radiation component in combustion simulations. Although some of these numerical solvers have been compared in the literature, a comprehensive accuracy and computational cost comparison of the three main types of radiation solvers – Discrete Ordinates Method (DOM), Spherical Harmonics Method (SHM), and the Photon Monte Carlo (PMC) method – has not been completed. Moreover, the most accurate method, the PMC method, is computationally cumbersome and expensive. Potential areas of improvement to the efficiency of the PMC method is an active field of research and is a primary motivation for this work.

1.2 Scope

As established in the previous section, radiative heat transfer is a significant component of high-fidelity combustion simulations. Negligence of radiation or vastly inaccurate radiation calculations can lead to large inaccuracies in results. Furthermore, radiation is difficult to model, and the most accurate radiation calculations are also computationally expensive. In this work, a detailed comparison of the three main types of radiation solvers will be performed. The three solvers will be tested on a single snapshot of a scaled-up Sandia Flame D, a flame that is widely used to validate combustion models in the literature. Both the computational cost and accuracy of each solver will be included in this comparison.

Additionally, a throrough investigation of the computational load of the PMC method will be conducted. A load distribution study of a finite-volume based PMC code will be used to compare computational load statistics with local variables like temperature, volume, and Planck

mean absorption coefficient. The results of the load distribution study could eventually be used to develop an a priori estimation of the load and to better distribute the computational load across multiple processors, improving the parallel efficiency of the PMC code. Specific investigation of ray bundling, a potential improvement to PMC calculations, will also be conducted.

1.3 Literature Review

The effect of thermal radiation in combustion simulations has been well-researched. First, I present a sampling of articles that investigate the effect of radiation in laminar flames. Zhu and Gore study the effect of radiation on numerical simulations of one-dimensional opposed-flow laminar methane-air diffusion flames [1]. It was found that radiation heat loss has significant effects on the prediction of pressure, temperature, soot and NO emissions, and pollutant mole fractions. Liu et al compare the effect of different radiation models on an axisymmetric laminar methane-air diffusion flame as well as the computational cost of different radiation models [2]. They conclude that use of an approximate radiation model affects predictions for temperature, species concentrations, soot information, and flame structure. Liu et al present findings on the effect of radiation in relatively small-scale diffusion flames at normal gravity and microgravity [3]. It was found that the impact of radiative transfer in conditions of microgravity are even more important than for similar simulations conducted at normal gravity. Other findings on the impact of radiation in combustion of laminar flames can be found in [4], [5], and [6].

Radiation is also found to be important in turbulent combustion simulations. Here, I present a sample of the literature on the radiation effect in turbulent combustion simulations. Bidi et al investigate the radiation effect in turbulent premixed methane-air combustion [7]. They found that the effects of radiative heat transfer on temperature and species concentration profiles, especially in regions of highly-emitting non-gray gases, is significant. They also report that the maximum flame temperature decreases when the radiation effect is considered. Two temperature profiles, one calculated with radiation and one calculated without radiation, are presented in Figure 1.1 [7]. The differences between the two temperature profiles are stark. Damien et al study the interaction of turbulent combustion and radiation by coupling large eddy simulation (LES) turbulence modeling with a radiation model that combines the discrete ordinate method (DOM) and a global spectral model [8]. They report significant radiation effects on the overall energy distribution, temperature profiles, and species concentrations in the flame, similar to the findings in [7]. They also find that radiative transfer impacts the overall flame structure and that

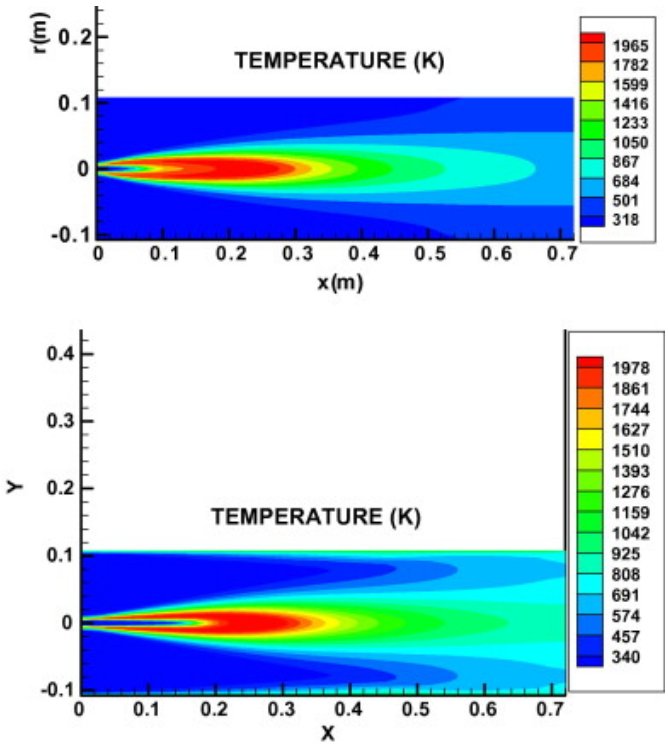

Figure 1.1: Two temperature profiles calculated without radiation (top) and with radiation (bottom) from [7]

turbulence radiation interaction (TRI) correlations must be considered in turbulent combustion simulations. Yin et al conduct a computational fluid dynamics (CFD) study on chemistry and radiation in oxy-fuel combustion [9]. One of the main objectives of their study was to implement and validate a new weighted sum of gray gases model (WSGGM) for gaseous radiative properties. The new WSGGM performs significantly better than the old, demonstrating the advantages of accurate radiation modeling. Yoshikawa and Reitz investigate the relationship between radiation and NO_x emissions in diesel engine combustion [14]. They report a reduction in NO_x and soot emissions as a result of radiation heat loss. Tkachenko et al study the interaction of radiation and turbulence on turbulence statistics and temperature distributions in convective channel flow [10]. They found that wall-to-wall radiation has significant effects on temperature values and that gas radiation has an impact on turbulent statistics throughout the flow. Other findings on TRI and the radiation effect in turbulent combustion simulations can be found in [11], [12], and [13].

Accurate radiation calculations also factor into the design of combustion components. Naraghi et al present a radiation model for liquid rocket engines [15]. They found that radiation significantly affects wall temperature, pressure drop of the coolant, and coolant Mach number.

These findings would necessitate changes to the design of the cooling system. Goebel et al present similar findings on the influence of radiation in modern rocket combustion that are a necessary consideration in the design process [16].

All in all, the literature supports the importance of accurate radiation modeling in high-fidelity combustion simulations. A comprehensive overview of radiation heat transfer in turbulent combustion simulations can be found in [17]. More detailed literature review of the specific areas of study that are covered in this work is detailed in later chapters.

1.4 Organization

First, a brief theoretical background of radiation, spectral models, and radiative transfer equation (RTE) solvers will be presented. Then, the computational cost and accuracy comparison of the DOM, SHM, and PMC method will be described with detailed results. Following that, the results of the PMC load distribution assessment and ray bundling investigation will be recounted. Final conclusions will be made, and a guide to future work will be suggested.

CHAPTER 2

THEORY

2.1 Introduction

Of the three primary forms of heat transfer, radiation is the most complex to model. Unlike conduction and convection, radiative energy travels by way of electromagnetic waves. The energy content of an electromagnetic wave depends on its wavenumber whose possible values range the entire electromagnetic spectrum. Radiation also varies with time, temperature, spatial location, and direction. Even in the most basic black body cases, radiation still has a highly nonlinear relationship with temperature. Thus, the contribution of radiation in combustion reactions becomes a difficult computation. In most combustion models, radiation is solved by combining a spectral model with an RTE solver. An RTE solver solves the governing equation of radiation for a single wavenumber, while a spectral model captures the variation of radiative properties with wavenumber. Implementing these two primary components, one solves for the divergence of the radiative heat flux, $\nabla \cdot \mathbf{q}_{\text{rad}}$, which is used as a source term in the energy equation given by [17]

$$\frac{\partial \rho h}{\partial t} + \frac{\partial \rho h u_i}{\partial x_i} = -\frac{\partial J_i^h}{\partial x_i} + \frac{Dp}{Dt} + \tau_{ij}\frac{\partial u_j}{\partial x_i} + S_{\text{rad}} \tag{2.1}$$

where x_i is the ith spatial coordinate, u_i is the ith component of velocity, h is the specific enthalpy of the medium, ρ is the density, p is the pressure, τ_{ij} is the viscous stress tensor, J_i^h is the ith component of the molecular flux of enthalpy, and S_{rad} is the radiative source term. The divergence of the heat flux and the radiative source term are related by the following equation:

$$S_{\text{rad}} = -\nabla \cdot \mathbf{q}_{\text{rad}}. \tag{2.2}$$

The divergence of the radiative heat flux $\nabla \cdot \mathbf{q}_{\text{rad}}$ will be referred to as $\nabla \cdot \mathbf{q}$ for the remainder of this work. All equations presented later in this chapter, unless otherwise noted, are taken from [18].

2.1.1 Radiative Transfer Equation

The radiative transfer equation (RTE) is an integro-differential equation that solves for radiative intensity (radiative energy flow per time per area normal to radiation direction per solid

angle) as it varies with time, temperature, spatial location, and direction. It is given by

$$\frac{1}{c}\frac{\partial I_\eta}{\partial t} + \frac{\partial I_\eta}{\partial r} = j_\eta - \kappa_\eta I_\eta - \sigma_\eta I_\eta + \frac{\sigma_\eta}{4\pi}\int_{4\pi} I_\eta(\hat{s}_i)\Phi_\eta(\hat{s}_i,\hat{s})\,d\Omega_i. \tag{2.3}$$

The variables for Equation 2.3 are defined as follows:

c = speed of light [m/s]

t = time [s]

r = position along a path [m]

$\hat{s}$ and $\hat{s}_i$ = unit direction vectors along a path [m]

η = wavenumber of radiation [m^{-1}]

I_η = intensity due to wavenumber η [W/m^2]

$j_\eta = \kappa_\eta I_{b\eta}$ = emission term [W/m^3]

κ_η = absorption coefficient of the medium at wavenumber η [m^{-1}]

$I_{b\eta}$ = Planck function or blackbody intensity at wavenumber η [W/m^2]

σ_η = scattering coefficient of the medium at wavenumber η [m^{-1}]

$\phi_\eta(\hat{s}_i,\hat{s})$ = phase function [-]

Ω_i = solid angle [sr]

$\sigma_\eta I_\eta$ = out-scattering term [W/m]

$\frac{\sigma_\eta}{4\pi}\int_{4\pi} I_\eta(\hat{s}_i)\Phi_\eta(\hat{s}_i,\hat{s})\,d\Omega_i$ = in-scattering from other directions [W/m].

One common simplification to the RTE is the quasi-steady approximation, which neglects the time derivative of I_η. The quasi-steady approximation assumes that the medium is at rest compared to the speed of light, which is a good approximation for most applications. Thus, the independent variable time t is removed, and Equation 2.3 is reduced to

$$\frac{dI_\eta}{dr} = j_\eta - \kappa_\eta I_\eta - \sigma_\eta I_\eta + \frac{\sigma_\eta}{4\pi}\int_{4\pi} I_\eta(\hat{\mathbf{s}}_\mathbf{i})\Phi_\eta(\hat{\mathbf{s}}_\mathbf{i},\hat{\mathbf{s}})\,d\Omega_i. \tag{2.4}$$

Each term on the right hand side of Equation 2.4 corresponds to an attenuation (decrease) or augmentation (increase) of radiative energy due to emission, absorption, or scattering. Analytical solutions to the RTE can only be found in very simple combustion configurations, so various numerical methods have also been developed to solve the RTE.

2.2 Numerical Solution Methods

The three commonly used types of numerical RTE models are the discrete ordinate method (DOM), the spherical harmonics method (SHM), and the photon Monte Carlo (PMC)

method. The DOM and SHM are both deterministic methods, while the PMC method is stochastic. These three methods vary in accuracy and computational cost.

2.2.1 Discrete Ordinates Method

The Discrete Ordinates Method (DOM) discretizes the directional variation of radiative intensity. Instead of a continuous function, the intensity is expressed as a finite number of partial intensities on a set of prescribed directions, called ordinates. Each partial intensity is multiplied by a corresponding quadrature weight and summed to calculate the radiative flux $\mathbf{q}$ or incident radiation G. Equation 2.4 is converted to

$$\frac{dI_{i\eta}}{dr} = j_{i\eta} - \kappa_{i\eta} I_{i\eta} - \sigma_{i\eta} I_{i\eta} + \frac{\sigma_{i\eta}}{4\pi} \sum_{j=0}^{n} I_{j\eta}(\hat{s}_j) \Phi_{i\eta}(\hat{s}_j, \hat{s}_i)\, d\Omega_i, \quad i = 1, 2, \ldots, N \tag{2.5}$$

where N is the total number of ordinates, i specifies the ordinate direction, $I_{i\eta}$ is the partial intensity in ordinate direction i at wavenumber η, and $\hat{s}_i$ is the ordinate direction specified by i. Therefore, Equation 2.4 is transformed into a set of N first-order partial differential equations. The equations for radiative heat flux $\mathbf{q}$ and incident radiation G for a single wavenumber η are given by

$$\mathbf{q}_\eta(r) = \int_{4\pi} I_\eta(r, \hat{\mathbf{s}}) \hat{\mathbf{s}} d\Omega \approx \sum_{i=1}^{n} w_i I_{i\eta}(r) \hat{\mathbf{s}}_\mathbf{i} \tag{2.6}$$

$$G_\eta(r) = \int_{4\pi} I_\eta(r, \hat{\mathbf{s}}) d\Omega \approx \sum_{i=1}^{n} w_i I_{i\eta}(r). \tag{2.7}$$

A detailed explanation of the DOM can be found in [18].

For complex geometries and a large number of ordinate directions, the DOM can become computationally expensive. However, for axisymmetric geometry, where relevant properties vary only radially and axially, simplifications can be made to reduce the computational cost. In [19], two boundary conditions for the DOM are proposed. The first boundary condition is the specularly reflective boundary condition. This condition maintains that every intensity that reaches a computational wedge boundary is reflected in the same way that light reflects off a mirror. The formulation for this can be found in [19]. The second boundary condition is the rotationally invariant boundary condition, derived from the rotationally invariant formulation of the RTE proposed in [19]. The rotationally invariant boundary condition is implemented in all DOM radiation calculations in this work.

In axisymmetric or rotationally invariant geometries, the RTE does not vary azimuthally as defined by a cylindrical coordinate system. Thus, in cylindrical coordinates, the intensity can be written as

$$I(r, z, \phi\ \theta, \gamma) = I(r, z, 0\ \theta, \gamma - \phi) \tag{2.8}$$

where r, z, and ϕ are the radial, axial, and azimuthal spatial coordinates and θ and γ are the polar and azimuthal directional coordinates. From the detailed derivation in [19], the rotationally invariant RTE in cylindrical coordinates for an emitting and absorbing medium at a single wavenumber is given by

$$\sin\theta\cos\beta\frac{\partial I_\eta}{\partial r} + \cos\theta\frac{\partial I_\eta}{\partial z} - \frac{\sin\theta\sin\beta}{r}\frac{\partial I_\eta}{\partial \beta} = \kappa I_{b\eta} - \kappa I_\eta \tag{2.9}$$

where $\beta = \gamma - \phi$ from Equation 2.8. The rotationally invariant formulation of the DOM method is easily extended to scattering and nongray mediums. This formulation with its corresponding boundary conditions detailed in [19] is implemented on OpenFOAM using a finite volume discretization scheme for wedge geometry containing a single azimuthal layer of cells.

2.2.2 Spherical Harmonics Method

The Spherical Harmonics Method (SHM) transforms the RTE into a system of elliptic PDEs. The radiative intensity, the solution to the RTE, is approximated as a truncated series of spherical harmonics. The new expression for intensity is given by

$$I(r, \hat{s}) = \sum_{l=0}^{\infty}\sum_{m=-1}^{l} I_l^m(r) Y_l^m(\hat{s}). \tag{2.10}$$

where $I_l^m(r)$ are intensity coefficients and $Y_l^m(\hat{s})$ are spherical harmonics, given by

$$Y_l^m = \begin{cases} cos(m\phi)P_n^m(cos\theta) & \text{for m} \geq 0 \\ sin(m\phi)P_n^m(cos\theta) & \text{for m} < 0 \end{cases} \tag{2.11}$$

where P_n^m are the associated Legendre polynomials.

The SHM can be implemented to an arbitrary order of accuracy by truncating the series at a maximum value of l, deemed N. When applying the SHM to a generic 3-D combustion problem, the RTE is transformed into $N(N+1)/2$ elliptic PDEs where the highest order derivative is N. Hence, the SHM can also be referred to as the P_N method or P_N approximation. A detailed mathematical formulation of the P_N method for a generalized 3-D geometry is given in [20]. Derived equations for the P_1, P_3, P_5, and P_7 approximations can also be found in [21].

For all P_N calculations that will be performed in this work, the geometries are axisymmetric or rotationally invariant, effectively making the problem two-dimensional. As stated before, relevant properties only vary radially and axially. So, a simpler P_N solver for axisymmetric geometries is used. A detailed formulation of the 2-D axisymmetric P_N method, including the full set of P_N governing equations and boundary conditions, is reported in [22]. This 2-D axisymmetric P_N method reduces the total number of PDEs and boundary conditions from $N(N+1)/2$ to $(N+1)^2/4$. The governing equations are derived by applying axisymmetric relations to the generalized 3-D formulation of the P_N method found in [20]. The boundary conditions are derived from Marshak's boundary conditions in the 3-D formulation of the P_N method [23]. The PDEs are then solved iteratively on OpenFOAM using the preconditioned conjugate gradient (PCG) algorithm described in [24].

Since the mathematical complexity of the P_N approximation increases quickly with order N, the simplified P_N (SP_N) approximation is also investigated in this work as a mathematically simpler approach to the SHM. The SP_N RTE equations, formulated in [25], extend the formulation of the SHM for a one-dimensional slab to three dimensions, resulting in a total of $2(N+1)$ elliptic PDEs instead of $(N+1)^2/4$ for the axisymmetric P_N formulation or $N(N+1)/2$ for the generalized 3D P_N formulation. These equations contain no cross-derivatives and are subject to "nearly-decoupled" Marshak boundary conditions, leading to a simpler radiation calculation. In this work, both SP_3 and SP_5 are used.

2.2.3 Photon Monte Carlo Method

As stated before, while the DOM and SHM are deterministic solution methods, the Photon Monte Carlo (PMC) method is stochastic. In the PMC method, a large number of "rays" or "photon bundles" of radiative energy are traced from their point of emission to their point of absorption or until they reach a computational boundary. The spatial location of the origin, direction, wavenumber, and path of each emitted photon bundle can all be determined by random number relations detailed in [18]. In a typical finite volume-based Monte Carlo solver, a statistically significant number of photon bundles with a predetermined amount of radiative energy are traced from emission to depletion. Then, the radiative source term is computed by subtracting the absorbed energy from the emitted energy within each finite volume cell.

In this work, a finite volume-based PMC code is used to compute the radiative source term for each finite volume cell. The minutiae of this solver are described in [26]. Farmer and Roy

also propose a quasi-Monte Carlo (QMC) method that is implemented as a user-defined option in the finite volume PMC code. In the PMC method, independent random numbers are generated. Contrarily, in the QMC method, a deterministic algorithm is used to generate a sequence of numbers that mimic random behavior in a "self-avoiding fashion." This sequence is termed as a low-discrepancy sequence (LDS). Results in [26] show that if a large enough sample of LDS numbers is used, the distribution across the sampling domain approaches uniformity in the same way that true random sampling does. Both the PMC and QMC methods are used in this work.

2.3 Spectral Properties

As stated above, radiation travels via electromagnetic waves. Thus, the range of possible wavenumbers of radiation spans the electromagnetic spectrum. The radiative properties of a medium, including emission, absorption, and scattering coefficients, can vary with the wavenumber of radiation, and these variations must be considered when solving the RTE. Spectral models can range in accuracy, mathematical complexity, and computational cost.

2.3.1 Gray Assumption

One simplifying assumption that can be made is the gray assumption. If a medium is assumed to be gray, radiative properties do not vary with the wavenumber of radiation. Instead, averaged values for radiative properties are used when solving the RTE. The RTE under the gray assumption is given by

$$\frac{\partial I}{\partial r} = j - \kappa I - \sigma I + \frac{\sigma}{4\pi} \int_{4\pi} I(\hat{s}_i)\Phi(\hat{s}_i, \hat{s})\, d\Omega_i. \tag{2.12}$$

A commonly used gray model is the Planck-mean absorption coefficient given by Equation 2.13.

$$\kappa_P = \frac{\int_0^\infty \kappa_\eta I_{b\eta} d\eta}{\int_0^\infty I_{b\eta} d\eta} = \frac{1}{I_b} \int_0^\infty \kappa_\eta I_{b\eta} d\eta \tag{2.13}$$

Once the averaged values are determined, the gray assumption significantly reduces the overall computational cost of a radiation solver. Since the gray assumption does not account for any variation in spectral properties, it is likely that accuracy will be sacrificed in the calculation of radiation.

2.3.2 Non-Gray Radiation

Though there are many types of spectral models that are used in radiation calculations, the two spectral models that are utilized in this work are the full-spectrum k-distribution (FSK) method and the line-by-line (LBL) model. Descriptions of other spectral models can be found in [18].

Line-by-Line Model

At the atomic level, emission and absorption is caused by electrons moving energy levels within an atom. These energy transitions cause changes in radiative intensity, producing spectral lines. The line-by-line (LBL) spectral model accounts for contributions to intensity from all spectral lines across the electromagnetic spectrum. Because of this, it is considered the most accurate spectral model. The LBL model requires detailed knowledge of the size and shape of each spectral line, and this information is provided by high-resolution spectroscopic databases, such as HITRAN [27] or HITEMP [28], which record the strengths and locations of individual lines on the spectrum. For P_N and DOM calculations, the LBL model requires an excessive computational cost because an RTE must be solved for each spectral line, resulting in millions of calculations. On the contrary, for PMC calculations, the LBL model can be applied without any additional computational cost. PMC LBL calculations, when used with a sufficiently large statistical sample of photon bundles, are considered "exact." For the benchmark solution in Chapter 3, the PMC RTE solver with the LBL spectral model will be used. Ren and Modest's hybrid selection scheme for wavenumber η is used for all PMC LBL calculations in this work [29].

Full Spectrum k-Distribution Method

Although the LBL spectral model is the most accurate, its computational cost can become excessive, especially for P_N and DOM RTE solvers. An alternative to the LBL model that does not require the same computational expense is the full-spectrum k-distribution (FSK) method. The FSK method utilizes a probability distribution that spans the electromagnetic spectrum. This distribution, termed as a k-distribution, is defined as

$$f_{\bar{\phi},T}(k\ \bar{\phi},T) = \frac{1}{I_b(T)} \int_0^\infty I_{b\eta}(T)\delta(k-\kappa_\eta(\bar{\phi})d\eta. \tag{2.14}$$

In this equation, $\bar{\phi}$ is a vector containing thermodynamic state-defining variables, T is the temperature, $I_b(T)$ is the Planck function at temperature T, δ is the Dirac-delta function, and $\kappa_\eta(\bar{\phi})$

is the absorption coefficient for wavenumber η at the thermodynamic state defined by $\bar{\phi}$. The cumulative full-spectrum k-distribution is given by

$$g_{\bar{\phi},T}(k\ \bar{\phi},T) = \int_0^k f_{\bar{\phi},T}(k'\ \bar{\phi},T)dk'. \tag{2.15}$$

which describes the fraction of the spectrum whose absorption coefficients fall below k. In Equation 2.14, it is clear that the k-distribution accounts for the spectral variation of the Planck function and the absorption coefficient. Thus, it is considerably more accurate to employ the FSK method than the gray assumption.

In this work, the FSK method is applied using a look-up table constructed by Wang et al [30]. This look-up table is valid for a mixture of CO_2, H_2O, and CO at a wide range of values for temperature and pressure. The g-distribution in Equation 2.15 is integrated using 8 quadrature points. The FSK look-up table is used for all nongray P_N and DOM calculations in this work.

CHAPTER 3

COMPARISON OF RTE SOLVERS IN A TURBULENT JET FLAME

This chapter gives a detailed comparison of the accuracy and computational cost of different RTE solvers. The discrete ordinate method (DOM), the spherical harmonics method (SHM), and the photon Monte Carlo (PMC) method are all evaluated. For each RTE solver, the divergence of the heat flux ($\nabla \cdot \mathbf{q}$) is calculated for a frozen-field snapshot of Sandia Flame D, a turbulent piloted jet flame with a Reynolds number of approximately 22,400 [31].

3.1 Literature Review

Detailed comparison of different radiation models is sparsely found in the literature. Pal et al compare the effect of different radiation models and turbulence-radiation interaction (TRI) on peak flame temperature, NO emission, and the radiative source term in combustion simulations of optically thin and optically thick flames [33]. Both P_N and DOM approximations are benchmarked against PMC LBL accuracy. For the P_N method, only P_1 and P_3 are assessed for accuracy and computational expense, and for the DOM, only 6×2 and 16×4 ordinates are evaluated. Pal et al found that for optically thin flames, all RTE solvers produce results at a similar level of accuracy. Thus, a computationally cheap radiation model like the P_1 RTE solver with the gray assumption should be used. On the contrary, for optically thick flames, the P_3 RTE solver yields results closest to PMC LBL accuracy at a fraction of the computational cost of DOM and PMC RTE solvers. In this work, P_N approximations up to P_7, simplified P_N models SP_3 and SP_5, and 2×4, 2×8, 4×4, 4×8, 4×16, 8×8, 8×16, and 16×32 ordinates for the DOM will be evaluated for computational cost and accuracy using PMC LBL results as a benchmark. QMC results will also be included. Therefore, a more comprehensive comparison of the accuracy and computational cost of RTE solvers is accomplished.

P_N and DOM RTE solvers have been evaluated separately in the literature. For example, Cai et al compare the accuracy and computational cost of P_1, P_3, and simplified SP_3 and SP_5 methods while also comparing the effects of different mixing models and spectral models on radiation calculations [34]. The performance of the DOM formulation used in this work is also detailed in [19]. Cai et al use 2×4, 4×8, 8×16, and 16×32 ordinates to compare the two sets of boundary conditions described in Chapter 2: specularly reflective and rotationally invariant. Yet, neither [34] nor [19] evaluate the accuracy and computational cost of the P_N and DOM RTE

solvers to the degree of detail that is reported in this work. A detailed description and performance evaluation of the QMC method is given by Farmer in [26]. It was found that QMC performs well when compared with PMC LBL results. Nonetheless, there is yet to be a comparison of the QMC RTE solver with other RTE solvers like DOM and P_N.

3.2 Results

For each RTE solver, the divergence of the heat flux, $\nabla \cdot \mathbf{q}$, is sampled at different axial locations. For each simulation, the RTE solver is run for one time step on a dedicated HPC cluster, and the total execution time is recorded as the compuational cost for the RTE solver. Each simulation is run five times, and the smallest computational cost is recorded. For a sufficiently large sample of photon bundles, the solution calculated using the PMC RTE solver and LBL spectral model is close to exact. Thus, results given by the PMC LBL solver with 2 million rays or photon bundles (10 statistical runs at 200,000 rays per run) are used as the benchmark of accuracy for all other RTE solvers.

3.2.1 Target Flame

Sandia Flame D is a turbulent piloted jet flame with a main jet diameter of $d_j = 7.2$ mm and a pilot diameter of $d_p = 18.2$ mm [31]. The jet composition is 25% methane and 75% air, while the pilot burns a mixture of C_2H_2, H_2, air, CO_2, and N_2 with an equivalence ratio of $\phi = 0.77$. The Sandia D flame is commonly used to verify the accuracy of combustion models owing to the meticulous experimental measurements available in [31].

Pal et al found that for optically thin flames such as the original Sandia D flame, the effect of radiation is small. Thus, a difference in the RTE solver will not affect results for variables like temperature and species mass fractions. In this work, the Sandia D flame is scaled up by a factor of 4 to better evaluate the differences in radiation models ($d_j = 28.8$ mm, $d_p = 72.8$ mm), and a snapshot of the flame is taken from [32]. Contour plots for scalar fields of relevant species mass fractions, temperature, and Planck mean absorption coefficient for the snapshot used in this work are shown in Figure 3.1.

The divergence of the heat flux $\nabla \cdot \mathbf{q}$ is sampled at three different axial locations: $z/d = 14.93$, $z/d = 29.79$, and $z/d = 44.65$, where z/d is the ratio of the axial location z to the diameter of the main jet d. A sample plot of $\nabla \cdot \mathbf{q}$ at axial location $z/d = 14.93$ is given by Figure 3.2. The mean value is plotted, and the standard deviation is used as the statistical error shown by

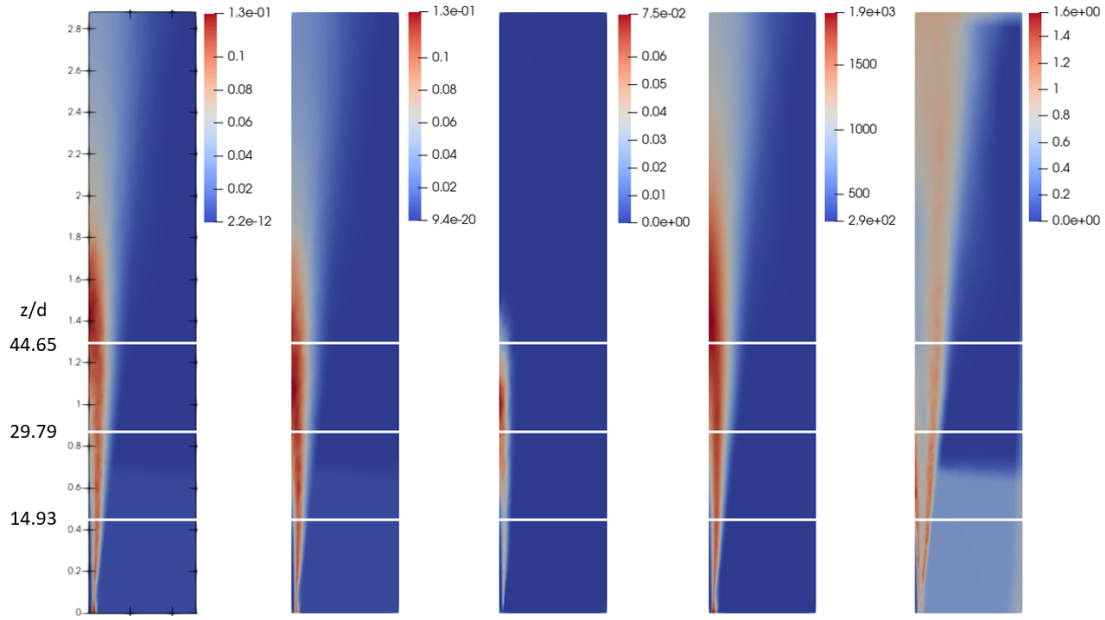

Figure 3.1: Scalar field values of Sandia D×4 for (left to right) CO_2 mass fraction, H_2O mass fraction, CO mass fraction, Temperature [K], and Planck mean absorption coefficient [1/m] with marked axial locations

the error bars in Figure 3.2.

3.2.2 RTE Solver Results

As stated in Chapter 2, the line-by-line (LBL) spectral model is generally the most accurate spectral model since every spectral line is accounted for. Additionally, it is stated that using the LBL spectral model in PMC calculations does not significantly add to the computational cost. Thus, PMC results shown in this chapter utilize the LBL spectral model to achieve the greatest level of accuracy. PMC LBL results are also used as a benchmark for accuracy.

If the LBL spectral model is used in conjunction with DOM or P_N RTE solvers, one would need to compute the solution to millions of RTEs. Because of this, the computational cost of the LBL spectral model becomes excessive. [30] shows that the FSK look-up table described in Chapter 2 produces LBL accuracy at a fraction of the computational cost. Thus, for all DOM and P_N RTE solvers that are used in this work, the FSK look-up table will be used as the primary spectral model.

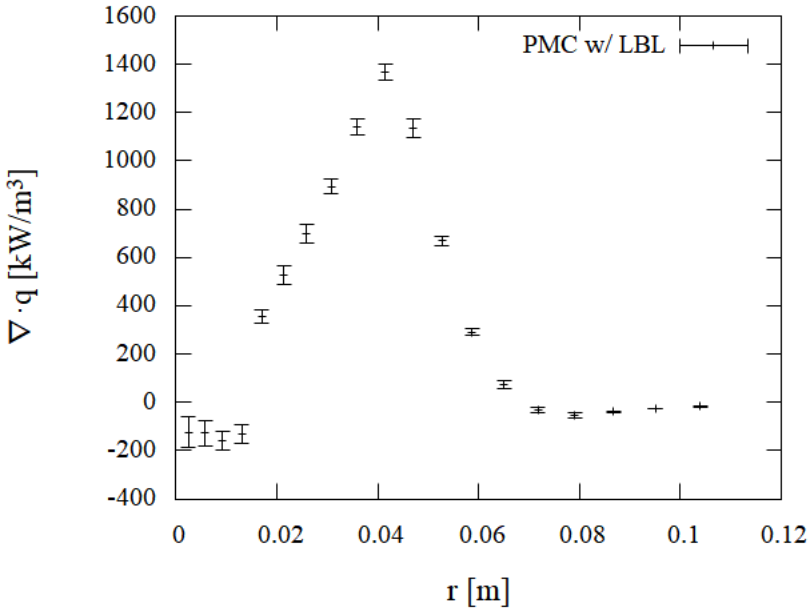

Figure 3.2: $\nabla \cdot \mathbf{q}$ at $z/d = 14.93$ for PMC LBL

SHM or P_N Results

The results for $\nabla \cdot \mathbf{q}$ for the P_1, P_3, P_5, and P_7 RTE solvers are compared with PMC LBL results in Figure 3.3. In general, for P_N results, a higher value of N corresponds to a higher level of accuracy. This is expected given the nature of the SHM described in 2.2.2. It is also shown that for most radial locations, except those greater than 0.1 meters, P_N RTE solvers tend to overpredict $\nabla \cdot \mathbf{q}$. The gain in accuracy also seems to lessen for each increase in N. For example, the gain in accuracy from P_1 to P_3 is larger than the gain in accuracy from P_3 to P_5. Furthermore, in this snapshot case, there is no visible gain in accuracy from P_5 to P_7.

Next, the performance of simplified P_N solvers SP_3 and SP_5 is evaluated. Figure 3.4 shows that both SP_3 and SP_5 perform reasonably well. SP_5 gives slightly more accurate results than SP_3. When compared with P_N results in Figure 3.4, SP_3 and SP_5 seem to yield a similar level of accuracy as the P_N RTE solvers with the same order of accuracy. For example, P_5 and SP_5 give siimlarly accurate values of $\nabla \cdot \mathbf{q}$ at the axial locations sampled in this work.

The computational cost for all P_N and SP_N RTE solvers is tabulated in Table 3.1. A plot of the computational cost versus the order of accuracy N for all P_N RTE solvers is also shown in Figure 3.5. Figure 3.5 shows a good R-squared value for a quadratic fit of the relationship between computational cost and order of accuracy N. This is consistent with the axisymmetric formulation

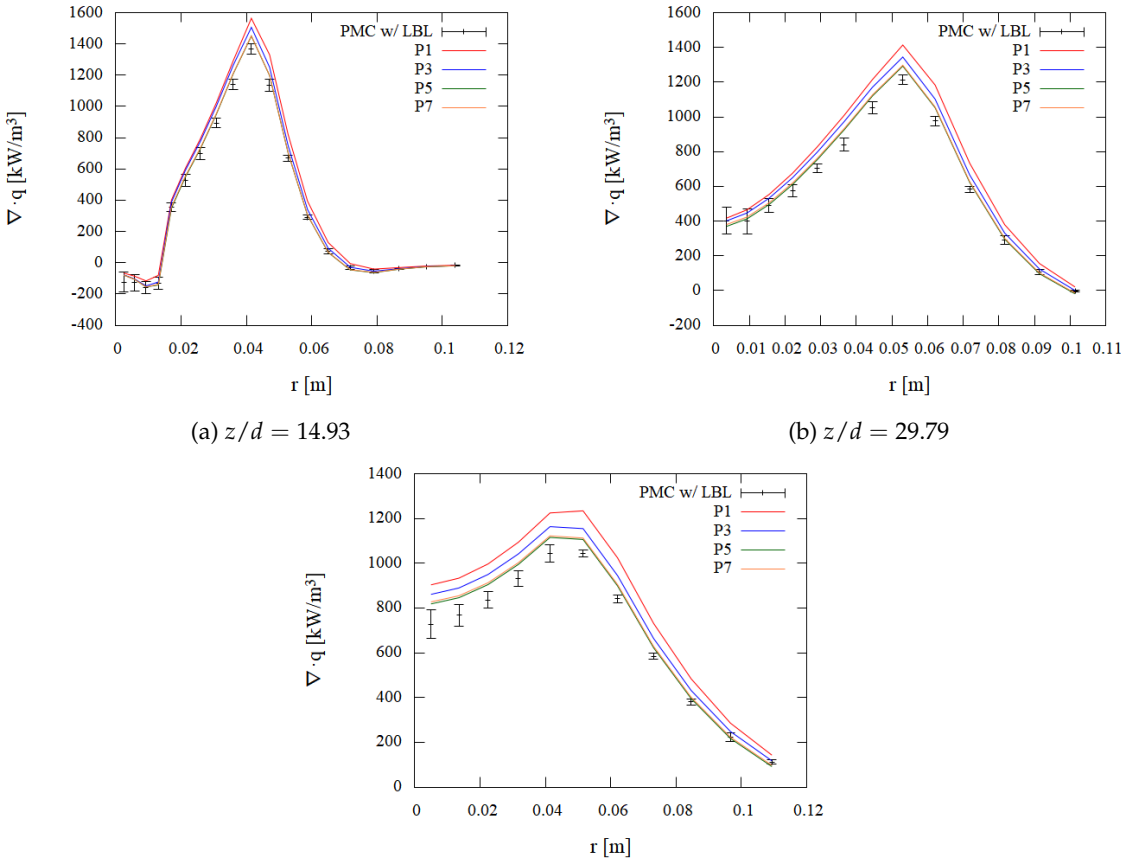

(a) $z/d = 14.93$

(b) $z/d = 29.79$

(c) $z/d = 44.65$

Figure 3.3: $\nabla \cdot \mathbf{q}$ for P_N with FSK table and PMC LBL

of the P_N approximation described in [22] which necessitates that for order of accuracy N, $\frac{(N+1)^4}{2}$ PDEs must be solved, suggesting a quadratic relationship between N and computational cost. Furthermore, each SP_N RTE solver has a slightly lower computational cost than the corresponding P_N RTE solver. For example, SP_3 has a slightly lower computational cost than P_3. Since all P_N solvers utilize the same spectral model, the differences in accuracy and computational cost can be attributed to the difference in RTE solver. In this case, the order of accuracy N determines the change in RTE solver.

DOM Results

For the DOM solver used in this work, the solid angle can be discretized in both the azimuthal (ϕ) and polar (θ) directions. In order to provide a comprehensive assessment of the accuracy and computational cost of the DOM, the number of ordinates in the azimuthal direction

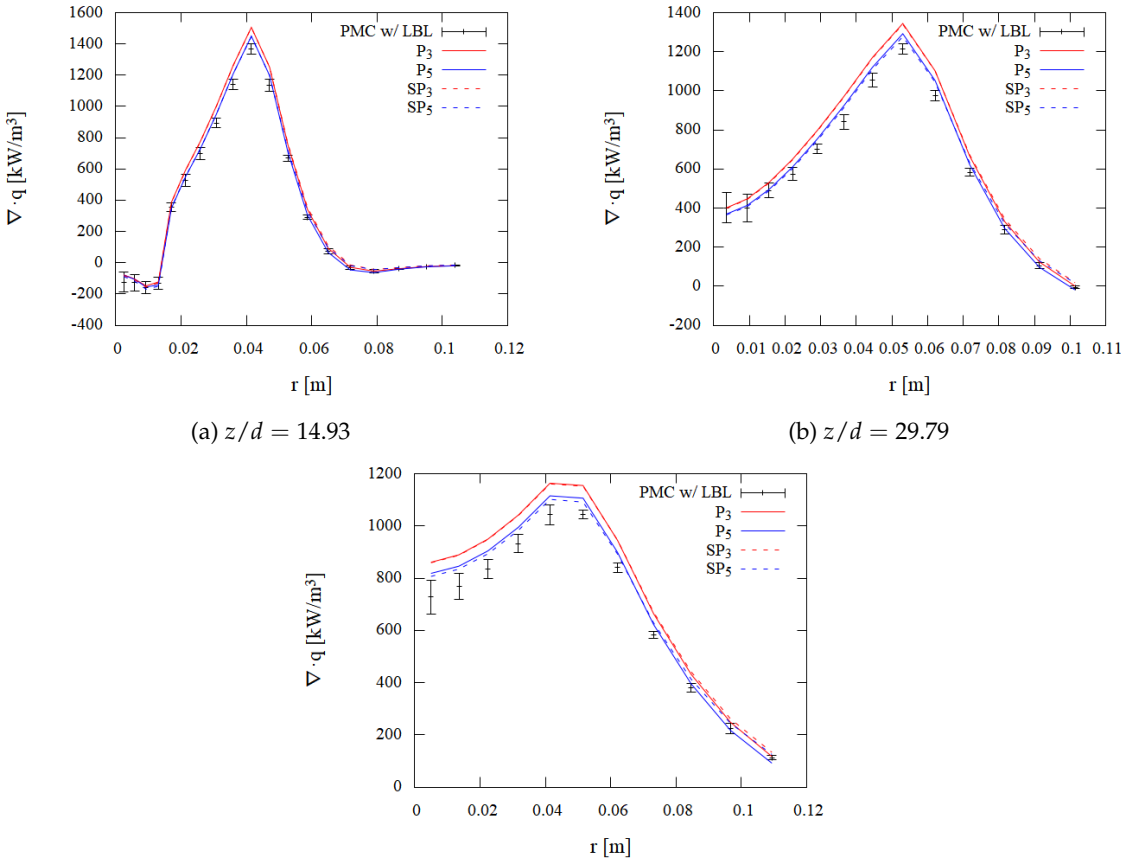

(a) $z/d = 14.93$

(b) $z/d = 29.79$

(c) $z/d = 44.65$

Figure 3.4: $\nabla \cdot \mathbf{q}$ for SP_3, SP_5, P_3, P_5 with FSK table and PMC LBL

Table 3.1: Computational cost for P_N RTE solvers with FSK table

RTE Solver	Computational Cost (s)
P_1	1.91
P_3	2.93
P_5	5.12
P_7	9.74
SP_3	2.47
SP_5	2.91

(n_ϕ), the number of ordinates in the polar direction n_θ, and the total number of ordinates ($n_\theta \times n_\phi$) are all varied. The results for $\nabla \cdot \mathbf{q}$ for 2×4, 2×8, 4×4, 4×8, 4×16, 8×8, 8×16, and 16×32 ordinates are compared with PMC LBL results in Figure 3.6. In general, a sufficiently high total number of ordinates yields adequately accurate values for $\nabla \cdot \mathbf{q}$. Moreover, at first glance, most

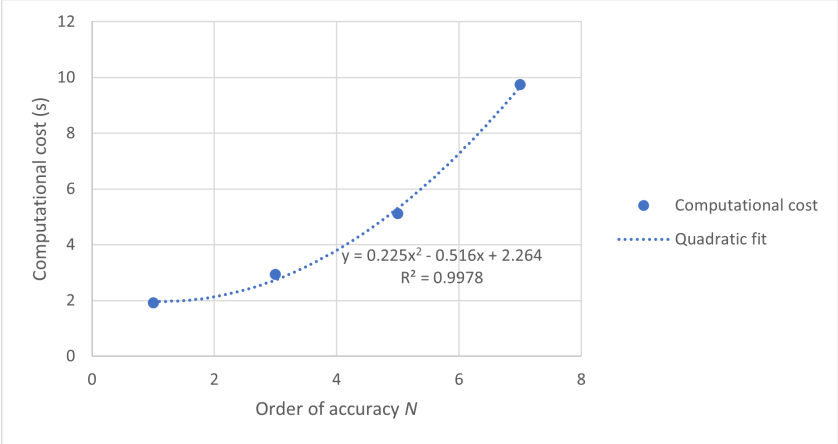

Figure 3.5: Computational cost vs. order of accuracy N for P_N RTE solver

DOM results seem to fall within the standard PMC LBL error except for higher numbers of ordinates at $z/d = 44.65$. Nonetheless, a more detailed evaluation of the effect of n_ϕ and n_θ on accuracy is required.

Figure 3.7 shows results for $\nabla \cdot \mathbf{q}$ given by 2×8 ordinates and 4×4 ordinates compared with PMC LBL accuracy. Although the total number of ordinates remains the same between the two ($2 \times 8 = 4 \times 4 = 16$), there remains a small but noticeable difference in accuracy. Results for all DOM RTE solvers from the centerline to a radius of approximately 0.04 meters where n_ϕ remains constant at $n_\phi = 8$ and n_θ varies are shown in Figure 3.8. Although an increase in n_θ shows a slight change in the value of $\nabla \cdot \mathbf{q}$, the difference is not significant. Results for all DOM RTE solvers for the same radius where n_θ remains constant at $n_\theta = 4$ and n_ϕ varies are shown in Figure 3.9. There is also a change in the value of $\nabla \cdot \mathbf{q}$ as n_ϕ increases, and this advantage in accuracy is more significant than the advantage in accuracy gained by an increase in n_θ. Conclusively, the impact on accuracy is greater for the number of azimuthal ordinates (n_ϕ) than the number of polar ordinates (n_θ) for the chosen figuration.

The relative computational cost for all numbers of ordinates is tabulated in Table 3.2. A plot of the computational cost versus the total number of ordinates is given in Figure 3.10. In general, the computational cost is proportional to the total number of ordinates. Figure 3.10 shows a good R-squared value for a linear relationship between the total number of ordinates and the computational cost. Also, Table 3.2 shows that DOM RTE solvers that use the same total number of ordinates require a similar computational cost (e.g. 4×16 and 8×8). Thus, the greater advantage in accuracy comes with using a higher number of ordinates in the azimuthal direction.

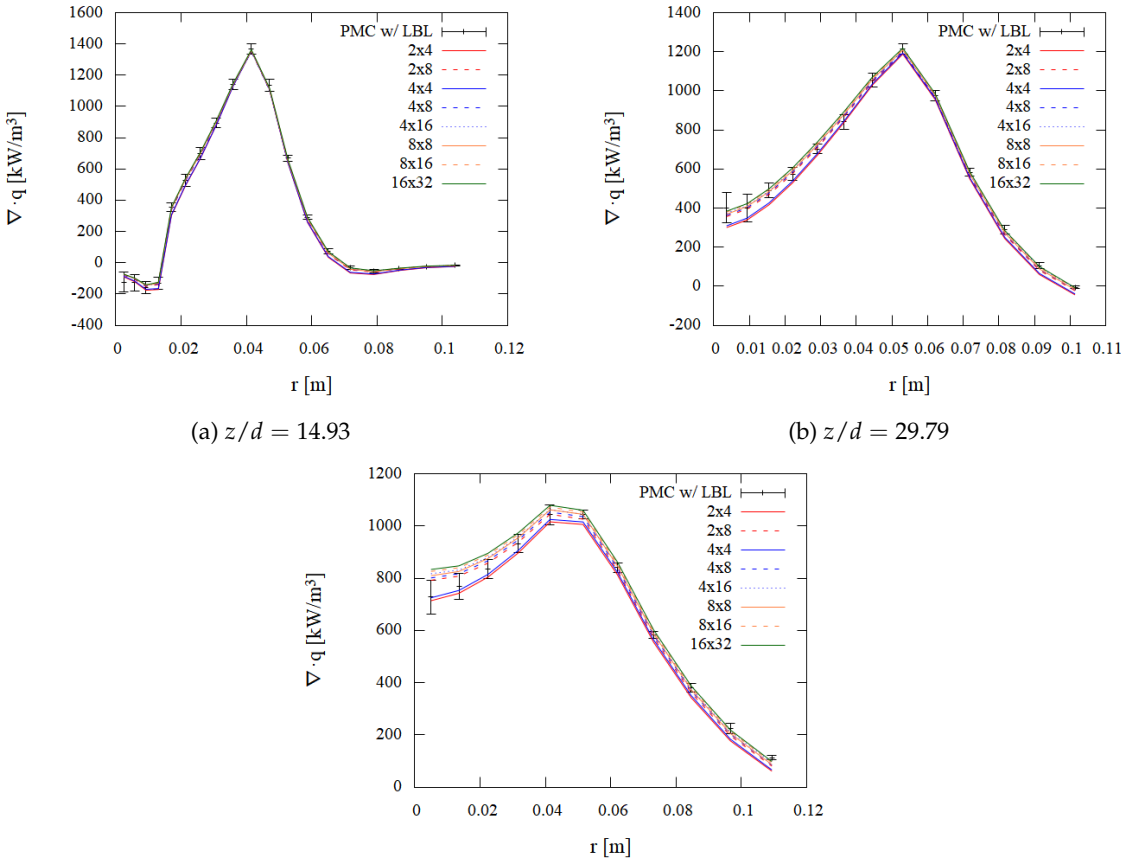

(a) $z/d = 14.93$

(b) $z/d = 29.79$

(c) $z/d = 44.65$

Figure 3.6: $\nabla \cdot \mathbf{q}$ for DOM with FSK table and PMC LBL

As stated in the previous section, all DOM RTE solvers use the same spectral model. Therefore, differences in accuracy and computational cost can be ascribed to the difference in RTE solvers. In this case, the total number of ordinates, the number of azimuthal ordinates n_ϕ, and the number of polar ordinates n_θ determine the change in RTE solver.

QMC Results

As detailed in Chapter 2, there exists an alternate version of the photon Monte Carlo (PMC) method called the quasi-Monte Carlo (QMC) method which uses low-discrepancy sequences (LDS) to simulate random number generation. Figure 3.11 shows QMC LBL and PMC LBL results side-by-side, and Table 3.3 shows the computational cost of each. For most axial locations, the values for $\nabla \cdot \mathbf{q}$ obtained using the QMC RTE solver fall within PMC LBL standard error. This is consistent with the description of the QMC method in Chapter 2. According to

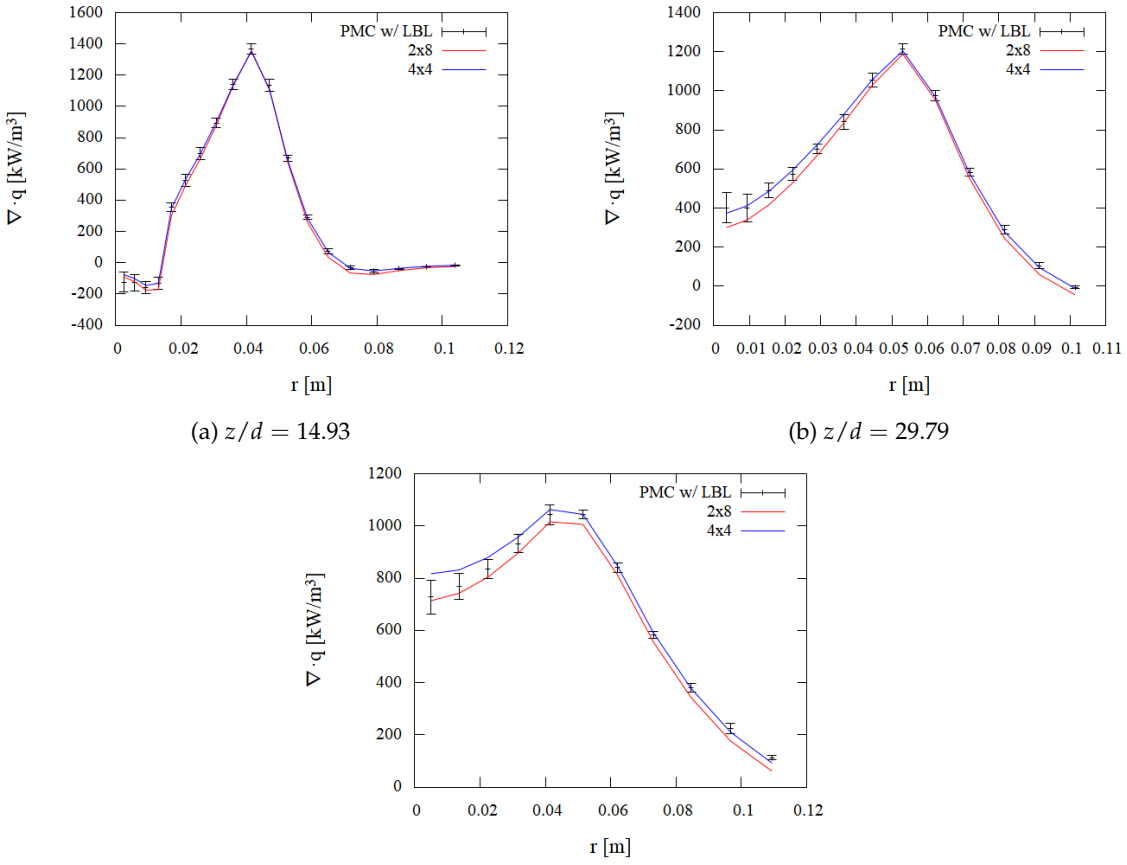

(a) $z/d = 14.93$

(b) $z/d = 29.79$

(c) $z/d = 44.65$

Figure 3.7: $\nabla \cdot \mathbf{q}$ for DOM with 2×8 and 4×4 ordinates and PMC LBL

Table 3.2: Computational cost for DOM RTE solvers with FSK table

RTE Solver	Computational Cost (s)
DOM 2×4	8.95
DOM 2×8	15.88
DOM 4×4	9.01
DOM 4×8	24.09
DOM 4×16	51.20
DOM 8×8	52.14
DOM 8×16	99.00
DOM 16×32	368.98

Chapter 2, a large enough sample of numbers obtained with an LDS approaches a uniform distribution, similar to true random behavior. As expected, the computational cost is significantly reduced when using the QMC method. Thus, the QMC method achieves sufficiently small error at

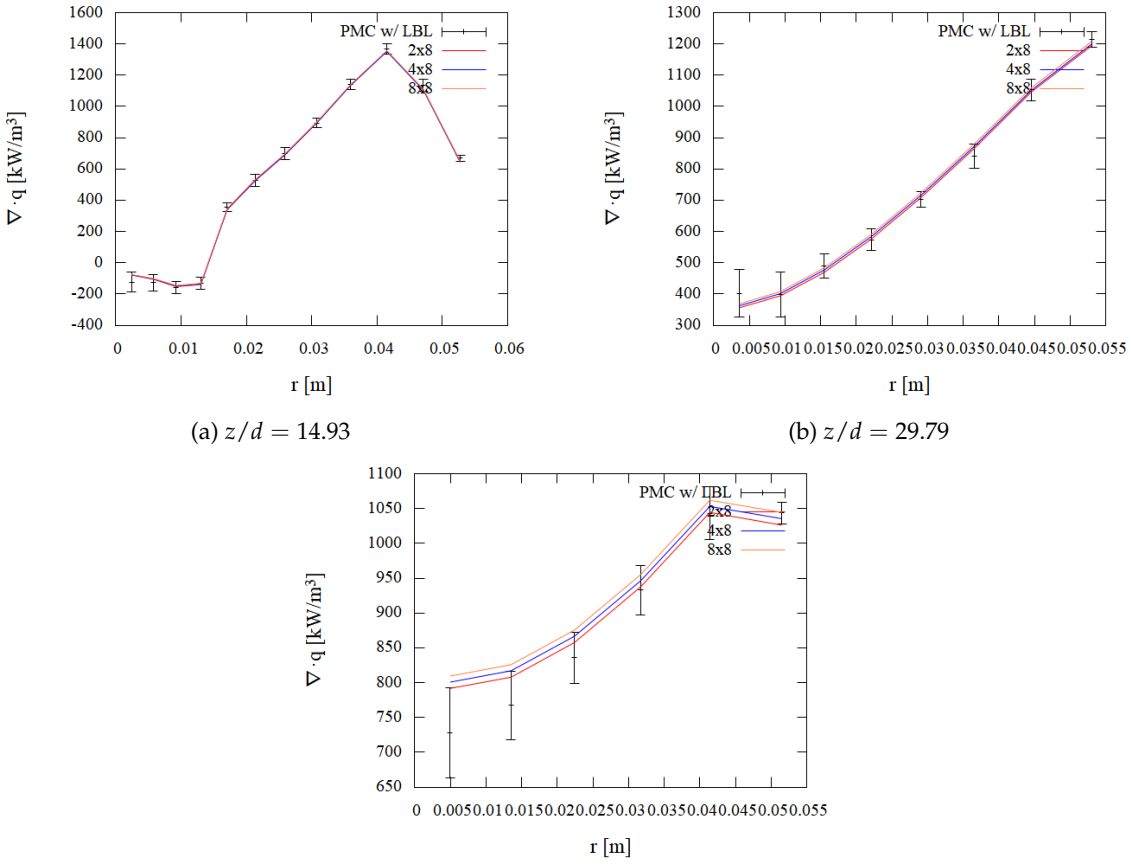

(a) $z/d = 14.93$

(b) $z/d = 29.79$

(c) $z/d = 44.65$

Figure 3.8: $\nabla \cdot \mathbf{q}$ for DOM with varying n_θ and PMC LBL

a lower number of rays. This is confirmed by the results in Table 3.3.

Table 3.3: Computational cost for PMC RTE solvers with LBL spectral model

RTE Solver	Computational Cost (s)
QMC (200,000 rays)	4.55
PMC (2 million rays)	32.66

Comparison of DOM, P_N, and QMC

In this section, the three alternatives to PMC RTE solvers (DOM, P_N, QMC) are briefly compared. P_7 and DOM with 4×4 ordinates are selected because their respective computational costs are approximately equal. The computational costs of P_7 and DOM with 4×4 ordinates are

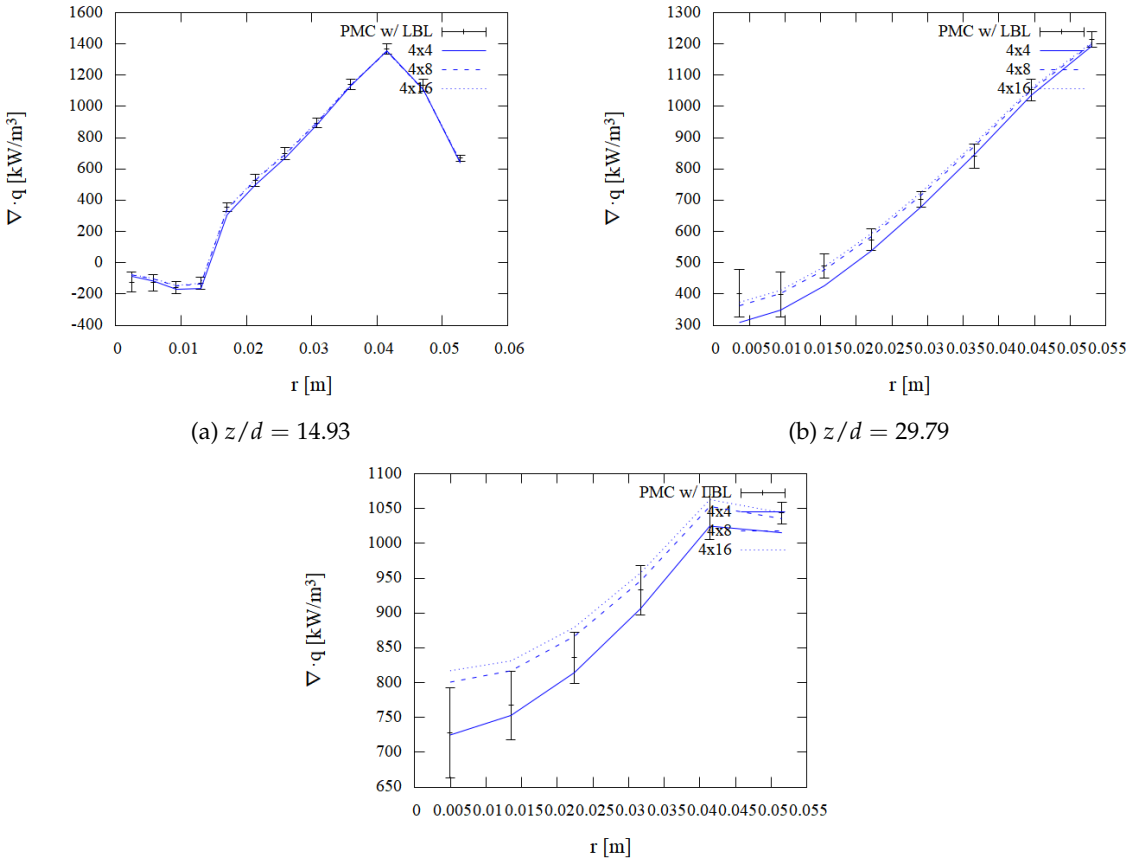

(a) $z/d = 14.93$

(b) $z/d = 29.79$

(c) $z/d = 44.65$

Figure 3.9: $\nabla \cdot \mathbf{q}$ for DOM with varying n_ϕ and PMC LBL

also on the same order as the computational cost of the QMC method. One should note that this comparison must be taken as an approximate comparison only. This is because there are many contributing factors to the overall execution time, and thus the computational cost, of each method. These factors could include the tolerances and number of iterations used in the numerical differential equation solvers implemented in OpenFOAM. Other implementation details of the RTE solver that may also impact the total execution time. A difference in any one of these factors could lead to different conclusions about the relative accuracy and computational cost of RTE solvers. Additionally, the computational cost of each RTE solver can be tuned by the user by changing the maximum number of iterations required by OpenFOAM's built-in numerical PDE solvers.

Figure 3.12 presents the divergence of the heat flux ($\nabla \cdot \mathbf{q}$) calculated using P_7 with FSK table, DOM (4×4) with FSK table, and QMC LBL. These results are also compared with PMC LBL

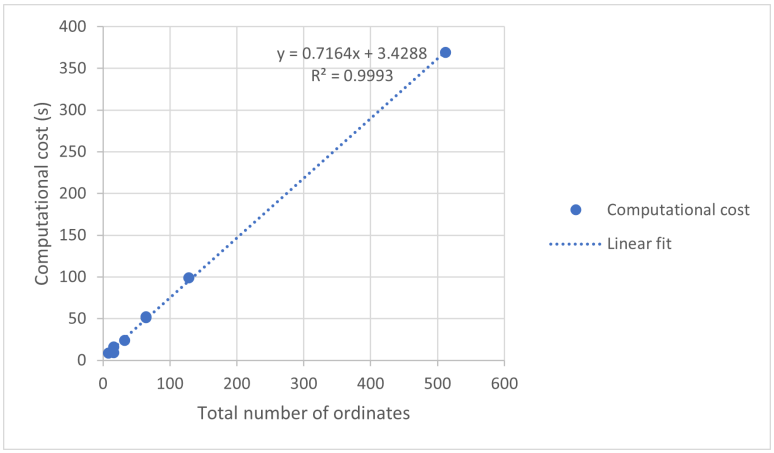

Figure 3.10: Computational cost vs. total number of ordinates $n_\theta \times n_\phi$ for DOM RTE solver

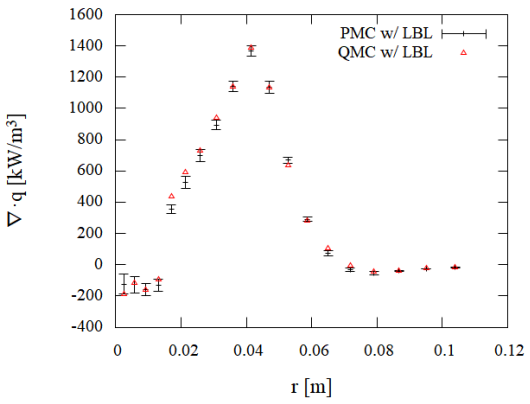

(a) $z/d = 14.93$

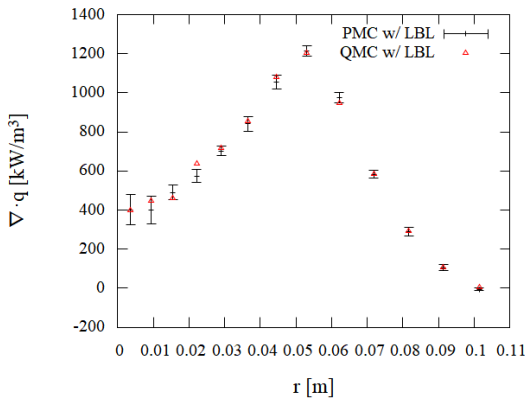

(b) $z/d = 29.79$

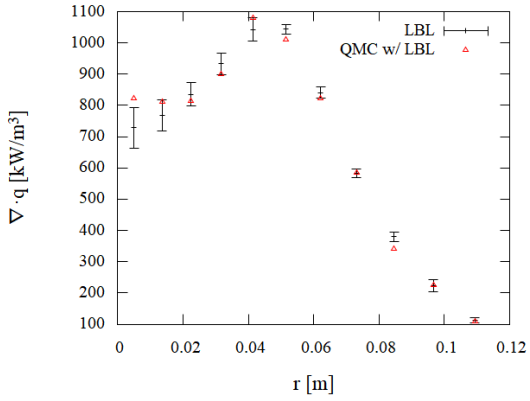

(c) $z/d = 44.65$

Figure 3.11: $\nabla \cdot \mathbf{q}$ for QMC LBL and PMC LBL

accuracy. In this figure, the P_7 results are notably less accurate than the DOM (4×4) results and the QMC results. Thus, in this specific case, the discrete ordinate method (DOM) and QMC perform better than the spherical harmonics method (SHM) at a similar computational cost. As stated before, the computational cost could be affected by other factors that are not simply the type of RTE solver used. Hence, this result cannot be applied for all combustion configurations.

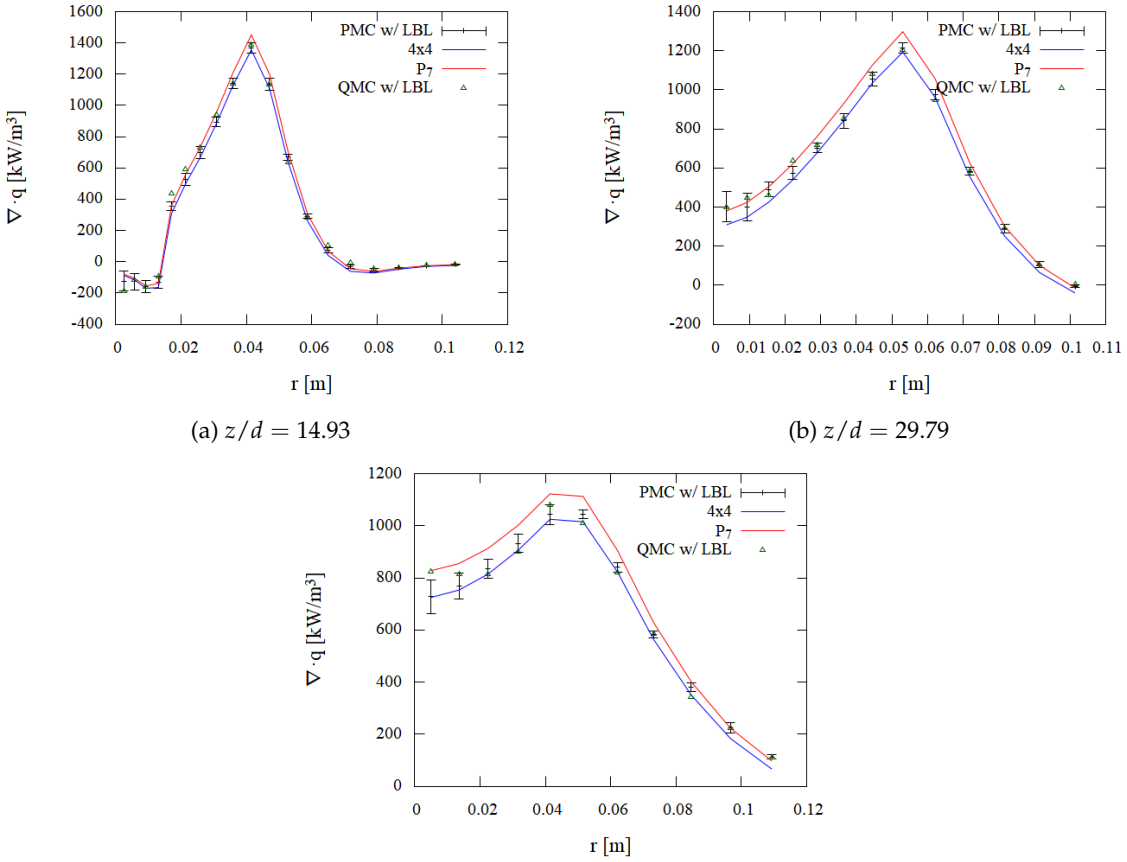

(a) $z/d = 14.93$

(b) $z/d = 29.79$

(c) $z/d = 44.65$

Figure 3.12: $\nabla \cdot \mathbf{q}$ for DOM, P_N, QMC, and PMC LBL

3.3 Discussion

In summary, P_N RTE solvers generally perform better with greater order of accuracy N, but the computational cost also increases quadratically with N. The increase in computational cost is expected as the axisymmetric P_N formulation solves $(N+1)^2/4$ elliptic PDEs. SP_N solvers perform similarly to the P_N solvers of the same order of accuracy (e.g. P_3 and SP_3). The

computational cost is reduced slightly when using SP_N solvers instead of P_N solvers. This follows from the fact that the P_N formulation in this work requires solutions to $\frac{(N+1)^2}{4}$ PDEs, while the SP_N formulation only requires solutions to $2(N+1)$ PDEs.

For the DOM, the accuracy of the RTE solver depends loosely on the total number of ordinates $n_\theta \times n_\phi$. However, the number of azimuthal ordinates n_ϕ affects the accuracy more than the number of polar ordinates n_θ. This is largely due to the thin wedge geometry of the problem. Because such a thin wedge angle is used, more azimuthal ordinates are needed to resolve all directions of intensity, consistent with results in [19]. In general, for locations closer to the center ($r = 0$), all DOM solvers perform well. However, for radial locations farther from the center ($r > 0.5$), those with lower numbers of ordinates slightly underpredict the divergence of the heat flux $\nabla \cdot \mathbf{q}$. These include 2×4 and 4×4 ordinates. The computational cost of DOM solvers also appears to be proportional to the total number of ordinates. This proceeds from the fact that the DOM solves $n_\theta \times n_\phi$ PDEs to compute $\nabla \cdot \mathbf{q}$.

Compared to PMC LBL, the QMC method performs very well. Most values of $\nabla \cdot \mathbf{q}$ fall within the standard error of PMC LBL results. Because of the nature of LDS sequences and the sufficient size of the sample of photon bundles, the QMC method is expected to perform well. Furthermore, the computational cost is a fraction of the cost of PMC LBL.

Overall, in this work, DOM seems to perform better than P_N in terms of accuracy. However, the current implementation of DOM is also notably more expensive than the P_N approximation. In Figure 3.12 where P_7 and DOM with 4×4 ordinates are compared side-by-side, DOM produces more accurate values for the divergence of the heat flux $\nabla \cdot \mathbf{q}$ than P_N. However, as stated before, the total execution time is recorded as the figure for computational cost. Since the total execution time factors in both the evaluation of the spectral model and the evaluation of the RTE and is affected by other implementation details of the RTE solver, differences in computational costs across different RTE solvers cannot always be attributed to the difference in RTE solvers. Additionally, both DOM and P_N can be tuned by changing the maximum number of iterations allowed for OpenFOAM's PDE solvers, which would also affect the total execution time of each simulation. On the other hand, QMC seems to perform better than both DOM with 4×4 ordinates and P_7, and the computational cost of QMC with 200,000 rays is about half the computational cost required by DOM with 4×4 ordinates and P_7. Thus, for this combustion configuration, QMC seems to perform the best while not requiring an excessively high computational expense like PMC normally requires.

Although these results are specific to a laboratory-scale turbulent-piloted jet flame and other similar types of flames, the Sandia D×4 flame provides a good representation of the radiation effect, and thus the importance of RTE solvers, in nonhomogenous participating media. Depending on the combustion configuration that is chosen, the results from this work could be used to select an RTE solver that meets the accuracy and computational cost requirements of the desired application.

CHAPTER 4

IMPROVEMENT OF PMC CALCULATIONS

This chapter explores the photon Monte Carlo (PMC) RTE solver in more detail. As stated in Chapter 2, the PMC RTE solver used in conjunction with the LBL spectral model produces the most accurate value of the divergence of the heat flux, $\nabla \cdot \mathbf{q}$. However, this method is also considerably more expensive than other RTE solvers like DOM and P_N. There remain areas of improvement to the efficiency of PMC calculations. Some of these areas of improvement will be investigated in this chapter, and others will be suggested in Chapter 6 for future avenues of exploration.

4.1 Literature Review

In the literature, there is a wide range of studies on improvements to Monte Carlo radiation calculations. One main category of these improvements is variance reduction methods, which attempt to decrease the statistical error of Monte Carlo calculations. One such variance reduction technique for surface-to-surface radiation calculations, called the control variate method, is discussed in [35]. This technique starts with the RTE given by Equation 2.4 and splits the radiative intensity I_η into a control intensity and a deviational intensity. The control intensity is selected to be the blackbody intensity at wavenumber η, $I_{b\eta}$, and can be calculated analytically. Thus, a Monte Carlo calculation is only needed to calculate the deviational intensity. Since the variance in the deviational intensity is expected to be smaller than the variance in the original intensity I_η, the overall variation of the Monte Carlo method should decrease. Another variance reduction technique for Monte Carlo transport calculations is investigated in [36]. This method is deemed MAGIC (Method of Automatic Generation of Importances by Calculation), and it seeks to predict the distribution of particles using information obtained from an initial analog run of the Monte Carlo transport code. The main objective in [36] of predicting the computational load distribution in Monte Carlo particle transport calculations is also an objective of this work. However, I seek to provide a correlation between local variables and computational load that does not require an initial run of the PMC code.

An improvement to the efficiency of Monte Carlo radiation transport calculations is suggested by [38]. In this study, a random walk procedure is derived to represent the absorption and reemission of radiation for one advance of spatial coordinates and time of a single particle.

This random walk procedure, especially in optically thick areas of the computational domain, is found to lower the computational cost of the Monte Carlo calculations without lowering the accuracy. A separate modification to PMC calculations is the implementation of low-discrepancy sequences (LDS) to simulate random number generation [26]. This method is called the quasi-Monte Carlo (QMC) method and has been described previously in this work. Any improvements discussed in this chapter are also applicable to QMC calculations.

No detailed work on the estimation of computational load in PMC calculations using local variables was found in the literature.

4.2 Assessment of Computational Load

For large and complicated combustion simulations, it is practical and sometimes necessary to parallelize PMC calculations in order to divide the computational load between processors. Thus, the finite volume-based Monte Carlo radiation code that is used in this work is capable of parallel calculations by decomposing the computational domain. The parallel efficiency of a calculation depends on how balanced the load is between processors. In other words, the more evenly the computational load is divided between processors, the better the parallel solver will perform. However, the domain decomposition that is implemented in this work evenly divides the physical domain between processors and does not account for the load distribution across the entire domain. Consequently, the computational load is often imbalanced between processors. In order to balance the load before running a simulation, it is necessary to find a way to predict the load distribution, which is a primary motivation of this work.

In this section, I attempt to find a correlation between the computational load and local variables like temperature, cell volume, and Planck-mean absorption coefficient. In PMC calculations, two types of computational load are most prevalent: emission and tracing. In an actual PMC calculation, the computational load attributed to emission consists of calculating an origin point, direction of emission, and wavenumber for each ray using random number relations [18]. In this assessment of computational load, I define the local emission load as the number of rays emitted from each computational cell, which can be directly attributed to the energy content of each cell. The energy content of each cell is proportional to $\kappa_p V T^4$ where κ_p is the local Planck-mean absorption coefficient, V is the cell volume, and T is the local temperature. The

calculation for the local emission load is given by

$$n_i = \frac{(\kappa_p V T^4)_i}{\sum_j^N (\kappa_p V_T^4)_j} n_{ray} \tag{4.1}$$

where n_i is the number of rays emitted by cell i (emission load for cell i), n_{ray} is the total number of rays, and N is the total number of finite volume cells.

The other contributor to computational cost is ray tracing. After a ray is emitted, it must be traced to the next cell face that it intersects. Then, the ray is followed through the next cell, depositing some of its energy into the cell, until the next intersection face is found. This process continues until the ray's energy is depleted. Tracing the intersection of a ray with faces of computational cells requires a computationally intensive geometric search. This geometric search constitutes the computational load attributed to tracing. I define the local tracing load as the number of times a finite volume cell is intersected by an incoming ray, which is also the measure of the number of times the ray-face intersection search subroutine is invoked for each cell. This type of load does not have a direct mathematical relationship with local variables. Thus, in this section, investigation will focus on prediction of the tracing load. Note that the absolute numerical values of emission and tracing load are somewhat arbitrary as they depends on the number of total rays (n_{ray}), the number of cells in the computational domain, and the combustion configuration itself. Hence, I will focus on assessment of emission and tracing load on a case-by-case basis and not generalized across all cases. Figure 4.1 shows a basic flowchart of the PMC code to further illustrate the difference between emission and tracing load.

In Figure 4.1, every time a ray is emitted (e.g. "Emit ray j"), the emission load for that cell is increased by 1. Every time the process "Find next cell face intersection" is performed, the tracing load of the next cell is increased by 1. Note that these "loads" do not directly provide a numerical value of CPU times; rather, they indicate how many times a block of subroutines were called in the PMC program.

4.2.1 Target Cases

To assess the computational load distribution on a wide breadth of combustion configurations, four atmospheric pressure cases and three high-pressure cases are studied.

Turbulent-piloted jet flame

The first atmospheric pressure configuration is the scaled-up Sandia D flame that is used to validate radiation models in Chapter 3, named `sandiaDx4`. A more detailed description of this turbulent-piloted jet flame and contour plots of the relevant scalar fields can be found in [31] and Chapter 2. The geometry of the flame is assumed to be axisymmetric, so the model is solved on a computational mesh for a wedge with a single azimuthal layer of finite volume cells totaling 3325. The snapshot is again provided by [32]. This case is solved using 200,000, 500,000, and 1 million rays.

OpenFOAM three-dimensional pool fire case

The second atmospheric pressure case that is studied is one of OpenFOAM's `fireFoam` solver tutorial cases called `smallPoolfire3D`. This simulation is run using a large-eddy simulation (LES) approach to turbulence and an "infinitely fast chemistry combustion model" [37]. A snapshot of this case is obtained by selecting a timestep, specifically t=0.5 seconds, where there is a noticeable presence of hot gases CO_2, CO, and H_2O. The temperature at the inlet is set to a constant value of 300 K. The computational domain is 1 m$\times$1 m$\times$1 m and is solved on a computational mesh of 216,000 finite volume cells. This case is solved using 2 million, 5 million, and 10 million rays.

Laboratory-scale turbulent pool fire

The third atmospheric pressure case studied in this work is a snapshot of an n-heptane turbulent pool fire case studied in [40], deemed `poolfire2`. The diameter of the pool is 7.1 cm, and the flame height is approximately 34.5 cm. This pool fire has strong tendency to soot; thus, radiation effects are important. The original simulation is conducted using an LES turbulence model using approximately 9.6 million cells coupled with chemistry and soot models that are detailed in [41]. The temperature at the inlet is set to a constant value of 300 K. The original computational domain was coarsened by mapping 9.6 million cells onto a new mesh with 216,000 cells for computational ease. This case is solved using 1 million, 2 million, and 5 million rays.

Flame cube

The final atmospheric pressure case is an artificial case with 490,000 finite volume cells, called `flameCube` in this work [42]. This case was artificially created to mimic a smooth flame-like

contour of combustion products and temperature. The artificially created scalar field emulates a stationary steady methane flame in a rectangular box of size 1.04 m $\times$ 1.04 m $\times$ 2.88 m. Radiation is solved using 10 million, 20 million, and 50 million rays.

High-pressure gas turbine

The first high-pressure configuration is a high-pressure gas turbine combustor based on the SGT-100 industrial gas turbine combustor found in [43]. The snapshot of this case is taken from a study by Ren et al [44], and in this work, it is referred to as `gasTurbine`. This simulation is run using a Reynolds-averaged simulation approach to turbulence and a partially stirred reactor turbulent combustion model [37]. The walls are set as black with fixed temperature values of 673 K. Combustion occurs at a pressure of approximately 16 atm. The case has a computational mesh of 15,718 finite volume cells and is solved using 200,000, 500,000, and 1 million rays.

OpenFOAM aachenBomb tutorial case

The second high-pressure case is one of OpenFOAM's `sprayFoam` solver tutorial cases called `aachenBomb`. This simulation is run using an RAS approach to turbulence and a partially stirred reactor turbulent combustion model [37], and a snapshot is taking at t=0.01 seconds. Similar to `gasTurbine`, combustion occurs at a high pressure of about 7.5 atm. The simulation also enforces a zero gradient boundary condition for the temperature at the walls, and the walls are set to be black. The computational domain is .02 m$\times$.1 m$\times$.02 m with a computational mesh of 168,100 finite volume cells. Radiation is solved using 20 million, 50 million, and 100 million rays.

Constant-volume spray combustion chamber

The final combustion configuration that is studied in this work is the high-temperature, high-pressure Spray-A configuration provided by Engine Combustion Network [45], referred to in this work as `sprayA`. The snapshot is taken from [46]. In this configuration, combustion occurs in a constant-volume combustion chamber. The fuel is liquid n-dodecane, injected as a pressurized spray. The simulation is run using an RAS turbulence model combined with a partially stirred reactor turbulent combustion model [37]. Combustion occurs at a pressure of approximately 60 atm. The walls are hot and black, set at a fixed value of 850 K. The computational domain consists of 12,800 cells, and 100,000, 200,000, and 500,000 rays are used.

4.2.2 Results

A majority of the computational cost of PMC calculations is contributed by ray tracing. Table 4.1 shows the relative computational cost of emission and tracing as well as the hot cell fraction for each combustion case. The hot cell fraction is defined as the percentage of cells whose energy content ($\kappa_P V T^4$) falls above the mean energy content for all cells within the computational domain. In general, tracing seems to contribute the majority of the overall computational cost of all PMC calculations. For a single combustion case, the ratio remains roughly constant, and the overall cost scales with the number of rays. However, the exact proportion of the computational cost that is taken up by tracing varies from case to case. This could be due to a number of factors. For combustion cases with a smaller hot cell fraction like `smallPoolfire3D` and `smallPoolfire` (see contour plots in Appendix A), the tracing time is approximately 15 times the emission time which is large compared to other cases. In general, it seems that the ratio of tracing to emission time is related to the hot cell fraction ratio. Combustion configurations with smaller hot cell fraction have a smaller percentage of the computational domain that is highly emitting, so rays will have a farther distance to travel before getting absorbed or reaching a computational boundary. Also, for high pressure cases, the ratio of tracing to emission time seems generally smaller than the same ratio for atmospheric pressure cases. This could follow from the fact that the hot cell fraction in high pressure cases is larger. This could also be due to the local optical thickness of the medium which mostly depends on Planck-mean absorption coefficient κ_p. In high pressure cases, the values for κ_p are, on average, larger than they are for atmopsheric pressure cases. Thus, emitted rays in high pressure cases are generally absorbed more locally. The computational time information in Table 4.1 allows one to eventually calculate the average computational load per cell in terms of seconds which would improve any correlation that is developed.

The load contributed by emission of rays can be calculated prior to running the Monte Carlo code. Thus, emphasis will be placed on the relationship between the tracing load and a priori variables including temperature, Planck-mean absorption coefficient, and cell volume. Because these variables can be used to directly predict the emission load, they are expected to play an important role in predicting the tracing load as well. In this work, the number of photon bundles or rays emitted by each cell is recorded as the emission load, and the number of times a cell is intersected by an incoming ray or photon bundle is recorded as the tracing load. Another

Table 4.1: Computational cost and hot cell fraction for all combustion configurations and number of rays

Number of rays	Emission time (s)	Tracing time (s)	Tracing-Emission Ratio	Hot Cell Fraction
`sandiaDx4`				
100,000	0.29	1.56	4.45	0.191
200,000	0.59	3.19	5.41	0.191
500,000	1.46	7.84	5.37	0.191
`smallPoolfire3D`				
2 million	5.70	81.89	14.37	0.027
5 million	14.64	204.60	13.98	0.027
10 million	27.35	362.09	13.24	0.027
`poolfire2`				
1 million	3.27	51.11	15.63	0.018
2 million	6.49	99.39	15.31	0.018
5 million	16.12	246.37	15.28	0.018
`flameCube`				
10 million	36.39	363.77	10.00	0.142
20 million	71.47	733.32	10.26	0.142
50 million	172.92	1807.64	10.45	0.142
`gasTurbine`				
200,000	0.54	3.75	6.94	0.389
500,000	1.44	10.00	6.94	0.389
1 million	2.80	19.41	6.93	0.389
`aachenBomb`				
20 million	22.97	129.59	5.64	0.339
50 million	58.13	344.99	5.93	0.339
100 million	111.30	648.92	5.83	0.339
`sprayA`				
100,000	0.23	0.77	3.35	0.503
200,000	0.46	1.52	3.30	0.503
500,000	1.15	3.83	3.33	0.503

variable that is considered in the load distribution study is the optical thickness of each cell. This is defined as the Planck-mean absorption coefficient κ_P multiplied by some length scale l. The length scale is defined as the diameter of the sphere of equivalent volume for each cell. Given a cell volume V, the length scale is $l = (\frac{3V}{4\pi})^{1/3}$.

To gain a wide breadth of understanding on the correlation between the tracing load and a priori variables in PMC calculations, the PMC code is run for multiple combustion configurations and varying total number of rays. Atmospheric pressure cases include the Sandia D$\times$4 flame `sandiaDx4`, OpenFOAM's tutorial case `smallPoolfire3D`, another poolfire case `poolfire2`, and artificial case `flameCube`. High pressure cases include OpenFOAM's tutorial case `aachenBomb`, combustion in a gas turbine chamber `gasTurbine`, and `sprayA`.

The correlation coefficients between values in this work are computed using a `python` postprocessing code. A linear regression analysis between tracing load and emission load, tracing load and optical thickness, and emission load and optical thickness is also performed.

Qualitative Assessment

Contour plots of temperature, Planck-mean absorption coefficient (κ_p), cell volume, emission load, and tracing load for `gasTurbine` are given in Figure 4.2, and contour plots for `sandiaDx4` are given in Figure 4.3. Contour plots of the other five combustion cases can be found in Appendix A. The contour plots were taken as an x-z plane center slice on Paraview.

In both `sandiaDx4` and `gasTurbine`, there is an observable correlation between the emission and tracing loads. A similar trend can be seen in the contour plots for other cases (see Appendix A). Since the emission load is directly proportional to $\kappa_p V T^4$ where κ_p is the Planck-mean absorption coefficient, V is the cell volume, and T is the absolute temperature, there are also some visible correlations between these three variables and the tracing load. For OpenFOAM tutorial cases like `aachenBomb` where the finite volume cells are cuboid and uniform in volume, there will naturally be no correlation between volume and tracing load (see Figure A.4 in Appendix A). Overall, the greatest observable trend is a similarity between the emission and tracing load distributions in all cases. However, it should be noted that in atmospheric pressure cases like `sandiaDx4`, the correlation is generally less obvious than in high pressure cases like `gasTurbine`, where the similarities between emission and tracing load distributions are more noticeable.

Histograms of volume, temperature, Planck-mean absorption coefficient, optical thickness, emission load, and tracing load for `sandiaDx4` and `gasTurbine` that depict the number of data points that fall within a certain range of values are found in Figures 4.4 and 4.5. The correlation coefficients between emission load, tracing load, optical thickness, and other local variables are also tabulated in Tables 4.2 and 4.3. Histograms and correlation results for the other cases can be found in Appendix A.

At first glance, the histograms show data sets that are imbalanced, especially `sandiaDx4`. An imbalanced data set indicates that most of the data points are skewed towards one end of the range or another. For example, in Figure 4.5, it is clear that most values for the emission load are on the low end of the range, with the highest frequency falling in the 0-5 range. This means that any correlation that is developed with the current data set will be skewed towards data points

Table 4.2: Correlation coefficient data for `gasTurbine`

Relation Variables	Correlation Coefficient
Emission Load - Optical Thickness	0.6055
Emission Load - kPlanck	0.0897
Emission Load - Temperature	0.2348
Emission Load - Volume	0.7606
Tracing Load - Optical Thickness	0.5467
Tracing Load - kPlanck	0.03333
Tracing Load - Temperature	0.2231
Tracing Load - Volume	0.6966
Tracing Load - Emission Load	0.9764

Table 4.3: Correlation coefficient data for `sandiaDx4`

Relation Variables	Correlation Coefficient
Emission Load - Optical Thickness	0.2594
Emission Load - kPlanck	0.1972
Emission Load - Temperature	0.4591
Emission Load - Volume	-0.1227
Tracing Load - Optical Thickness	0.1999
Tracing Load - kPlanck	-0.0713
Tracing Load - Temperature	0.1322
Tracing Load - Volume	0.2733
Tracing Load - Emission Load	0.6767

with extremely low emission values. This extends to other imbalanced variables like tracing load and κ_p. The data sets for `gasTurbine` and other high pressure cases appear more balanced than the data sets for `sandiaDx4` and other atmospheric pressure cases (see Figures 4.4 and 4.5 and Appendix A). Table 4.2 shows a high correlation coefficient between tracing and emission loads at around 0.98. Table 4.3 also shows the highest correlation coefficient to be between tracing and emission loads at around 0.68, which is much lower than the tracing-emission correlation coefficient for `gasTurbine`. For other high pressure cases, there is a high correlation between tracing and emission loads, and for other atmospheric cases, the correlation coefficient between tracing and emission loads is moderately high (see Appendix A). These correlation coefficient values confirm the visible similarities that are seen between the tracing and emission loads in the contour plots (see Figures 4.3 and 4.2 and Appendix A). Computational cost information for emission and tracing for all cases are tabulated in Table 4.1.

Linear Regression

For each combustion case, three scatter plots are presented: tracing load vs. emission load, tracing load vs. optical thickness, and emission load vs. optical thickness. In each case, the tracing and emission loads have been scaled with the number of rays used in each simulation divided by 100,000 (i.e. 100, 200, and 500 for `flameCube`) and the hot cell fraction which was defined previously. The tracing and emission loads have first been normalized by the number of rays because each combustion configuration was run for three different numbers of rays. The loads have also been normalized by the hot cell fraction so that the range of values are consistent between different combustion cases. The new load L_i for cell i would be given by

$$L_i = \frac{100,000 * L_i^0}{n_{ray} h} \tag{4.2}$$

where L_i^0 is the non-normalized load in cell i, h is the hot cell fraction, and n_{ray} is the total number of rays used. The scatter plots can be found in Figures 4.6 through 4.12.

The high pressure cases, `gasTurbine`, `aachenBomb`, and `sprayA`, are presented first. In these cases, a linear regression represents the relation between emission and tracing loads fairly well. Each high pressure case gives an R-squared value of at least 0.8, suggesting a strong linear dependence of tracing load on emission load. For the high pressure cases, the scatter plots for tracing load vs. optical thickness and emission load vs. optical thickness show similar distributions and a relatively low correlation between either type of load and optical thickness with R-squared values ranging from 0.285 to 0.659.

The atmospheric pressure cases, `sandiaDx4`, `flameCube`, `poolfire2`, and `smallPoolfire3D`, are presented next. In these cases, the correlation between the tracing load and the emission load is much worse with R-squared values ranging from 0.451 to 0.612, excluding a good R-squared value of approximately 0.85 for the artificial case `flameCube`. Both `sandiaDx4` and `flameCube` show extremely low correlations between the tracing and emission loads and the optical thickness, with R-squared values ranging from 0.028 to 0.137. On the other hand, the `poolfire2` and `smallPoolfire3D` cases show slightly higher correlations between tracing and emission loads, tracing load and optical thickness, and emission load and optical thickness.

The best relationship shown by the scatter plots is still tracing and emission loads. However, in most atmospheric pressure cases, the correlation is much worse than for high pressure cases, and the optical thickness does not offer a good prediction of either tracing or

emission loads.

4.2.3 Discussion

Qualitative analysis of the contour plots for all combustion cases show a noticeable similarity between emission and tracing load distributions. Since emission is calculated directly from the volume, Planck-mean absorption coefficient, and temperature of each cell, there are some notable similarities between these three variables and the tracing load distributions as well. This makes sense given the nature of the PMC method. Cells that are neighboring highly emitting cells are likely to experience high tracing loads as well. Since the highly emitting cells in most cases are concentrated in certain parts of the domain, the cells with high tracing loads will also most likely be concentrated in a particular area of the domain. It is also expected that the tracing load distribution may be more spread out than the emission load distribution since emitted rays, more often than not, travel beyond the borders of their origin cells, sometimes crossing into areas of the domain that are not highly emitting.

However, although there is a visible similarity between emission and tracing load distributions, the actual correlation data does not support a strong enough relationship between the two variables for all combustion cases. For high pressure cases and for the artificial case `flameCube`, the correlation values are reasonably strong, and the scatter plots of tracing vs. emission loads in Figures 4.6, 4.7, 4.8, and 4.10 show R-squared values of at least 0.8. However, for the other atmospheric pressure cases, the correlation values are weak, and the scatter plots show very low R-squared values (see Figures 4.9, 4.11, 4.12). As shown in the histogram plots for κ_p, the average value for the Planck-mean absorption coefficient and overall distribution of Planck-mean absorption coefficient values is much higher for high pressure cases. This would make regions of high Planck-mean absorption coefficient more optically thick. Thus, rays or photon bundles would tend to be absorbed more locally to where they were emitted. This would lead to a better prediction of tracing load using the emission load. Therefore, for high pressure cases, a direct correlation between the tracing and emission load can be drawn. Although this correlation may not be exact, it could be used to predict the overall load distribution and balance the load between processors by decomposing the domain accordingly. Still, this correlation does not apply for most atmospheric cases. Moreover, for the artificial case `flameCube`, the optical thickness cannot be used as a justification as to why the correlation between the emission loads and tracing loads is good. For atmospheric pressure cases, more investigation is needed to find a suitable correlation

between the tracing load and local variables.

4.3 Ray Bundling

Another feature of the Monte Carlo code used in this work is the user option to trace multiple wavenumbers per ray or photon bundle. This feature is expected to decrease the overall computational cost of PMC calculations using the same total number of wavenumbers. This is because the same random number sequence can be used to trace the path of multiple wavenumbers instead of one, thereby reducing tracing by a factor of however many wavenumbers are traced per ray. Since tracing contributes the most to the overall computational cost of a PMC calculation, this should significantly reduce the overall computational cost. However, there is expected to be a trade-off in the accuracy or variance of the PMC method. This is because the randomness of the PMC calculation is lowered if more than one wavenumber is traced per ray. This would increase the statistical error of the PMC calculation. The impact of this feature on the accuracy and computational cost of the PMC method will be explored in this section in order to find an optimized value for the number of wavenumbers per ray.

4.3.1 Results

Snapshot cases of both `gasTurbine` and `sandiaDx4` are run to see the effects of changing the number of wavenumbers per ray or photon bundle. For both combustion cases, the total number of wavenumbers (number of wavenumbers per ray $\times$ number of rays) remains the same. 500,000 total wavenumbers are used for `sandiaDx4`, and 1 million total wavenumbers are used for `gasTurbine`. The plots of $\nabla \cdot \mathbf{q}$ and the standard deviation or statistical error of $\nabla \cdot \mathbf{q}$ for `gasTurbine` are found in Figures 4.13 through 4.17, and the corresponding plots for `sandiaDx4` are found in Figures 4.18 through 4.20. The minimum, maximum, and mean values of the standard deviation of $\nabla \cdot \mathbf{q}$ for all cells in the domain for `gasTurbine` and `sandiaDx4` are found in Tables 4.4 and 4.5 respectively. Finally, the computational cost for `gasTurbine` and `sandiaDx4` while varying the number of wavenumbers per ray is found in Tables 4.6 and 4.7 respectively.

Observing Figures 4.13 through 4.20, for both `gasTurbine` and `sandiaDx4`, changing the value of the number of wavenumbers per ray does not change the mean values of $\nabla \cdot \mathbf{q}$ by any significant amount. However, they also show a noticeable difference in the statistical error of the PMC calculation at the sampled loactions. On average, when increasing the number of wavenumbers per ray and holding the total number of wavenumbers constant, the statistical error

Table 4.4: Standard deviation of $\nabla \cdot \mathbf{q}$ statistics for `gasTurbine` (All units in kW/m^3)

	1×1M	2×500,000	4×250,000	5×200,000
Minimum	26.07	20.12	20.91	20.75
Maximum	14,132.98	20,709.70	19,383.49	22,986.37
Mean	1174.79	1485.45	1915.59	2095.29

Table 4.5: Standard deviation of $\nabla \cdot \mathbf{q}$ statistics for `sandiaDx4` (All units in kW/m^3)

	1×1×500,000	2×250,000	4×125,000	5×100,000	10×50,000
Minimum	2.44×10^{-12}	2.24×10^{-12}	4.03×10^{-12}	3.64×10^{-12}	3.40×10^{-12}
Maximum	84.33	90.87	110.06	131.38	193.28
Mean	6.57	7.72	9.72	10.47	13.80

Table 4.6: Computational costs for varying number of wavenumbers per ray for `gasTurbine`

	1×1M	2×500,000	4×250,000	5×200,000
Emission	26.43	19.92	16.32	15.88
Tracing	178.74	147.18	118.44	112.33
Total	246.27	193.93	154.30	146.38

Table 4.7: Computational costs for varying number of wavenumbers per ray for `sandiaDx4`

	1×500,000	2×250,000	4×125,000	5×100,000	10×50,000
Emission	14.60	11.35	9.55	9.08	7.78
Tracing	78.56	61.45	48.65	45.29	37.18
Total	105.52	79.49	62.00	57.67	47.14

also increases. This is confirmed by Tables 4.4 and 4.5. The mean value of the standard deviation of $\nabla \cdot \mathbf{q}$ for both `gasTurbine` and `sandiaDx4` increases with increasing number of wavenumbers per ray. With a few exceptions, the minimum and maximum values follow suit. Thus, the statistical error of the PMC calculation tends to increase with an increase in the number of wavenumbers per ray while holding the total number of wavenumbers constant. However, the mean value of $\nabla \cdot \mathbf{q}$ is relatively unaffected.

Tables 4.6 and 4.7 show that the computational cost of the PMC method decreases if the number of wavenumbers per ray increases while holding the total number of wavenumbers

constant. This holds true for separate emission and tracing times as well as the total execution time. To find an approximate optimized value for the number wavenumbers per ray, the computational cost and mean standard deviation of $\nabla \cdot \mathbf{q}$ were plotted against the number wavenumbers per ray. These plots are given by Figures 4.21 and 4.22.

It is assumed that the optimized value for the number of wavenumbers per ray is achieved where the two curves for computational cost and standard deviation of $\nabla \cdot \mathbf{q}$ meet. For `sandiaDx4`, this occurs around three wavenumbers per ray, and for `gasTurbine`, this occurs around two wavenumbers per ray. For larger numbers of wavenumbers per ray (i.e. 4 or greater), the sharp increase in the statistical error may not be worth the savings in the computational cost. Still, an increase from one to two wavenumbers per ray causes about a 25% decrease in the computational cost while increasing the statistical error by less than 10%.

4.3.2 Discussion

Changing the number of wavenumbers per ray or photon bundle affects both the computational cost and the accuracy of the PMC method. An increase in the number of wavenumbers per ray while holding the total number of wavenumbers constant causes an increase in the statistical error of the PMC method. This follows from the fact that in order to hold the total number of wavenumbers constant, the number of rays that are emitted and traced in a statistical run are decreased. Consider the example of two wavenumbers per ray. Instead of two wavenumbers following two separate paths that are determined by two different random number sequences, the wavenumbers are emitted and traced together. In essence, some of the samples are now correlated with each other. Thus, the randomness of the method is decreased, therefore increasing both the standard deviation and the variance of the statistical method.

The advantage of increasing the number of wavenumbers per ray is found in the computational cost, which decreases as the number of wavenumbers per ray increases. This can also be concluded from the fact that the number of rays must decrease in order to hold the total number of wavenumbers constant. Theoretically, tracing and overall execution time should be almost cut in half when the number of wavenumbers per ray is doubled. While this is not the case for the `gasTurbine` and `sandiaDx4` results shown in this work, there is a noticeable decrease in computational cost with an increase in the number of wavenumbers per ray. Furthermore, an optimal value for the number of wavenumbers per ray is achieved at around two or three wavenumbers ray. For one wavenumber per ray, the computational cost is significantly higher,

but for a higher number of wavenumbers per ray, the statistical error of the PMC calculation increases dramatically. These findings could be used to tune the number of wavenumbers per ray for the required application in future combustion simulations.

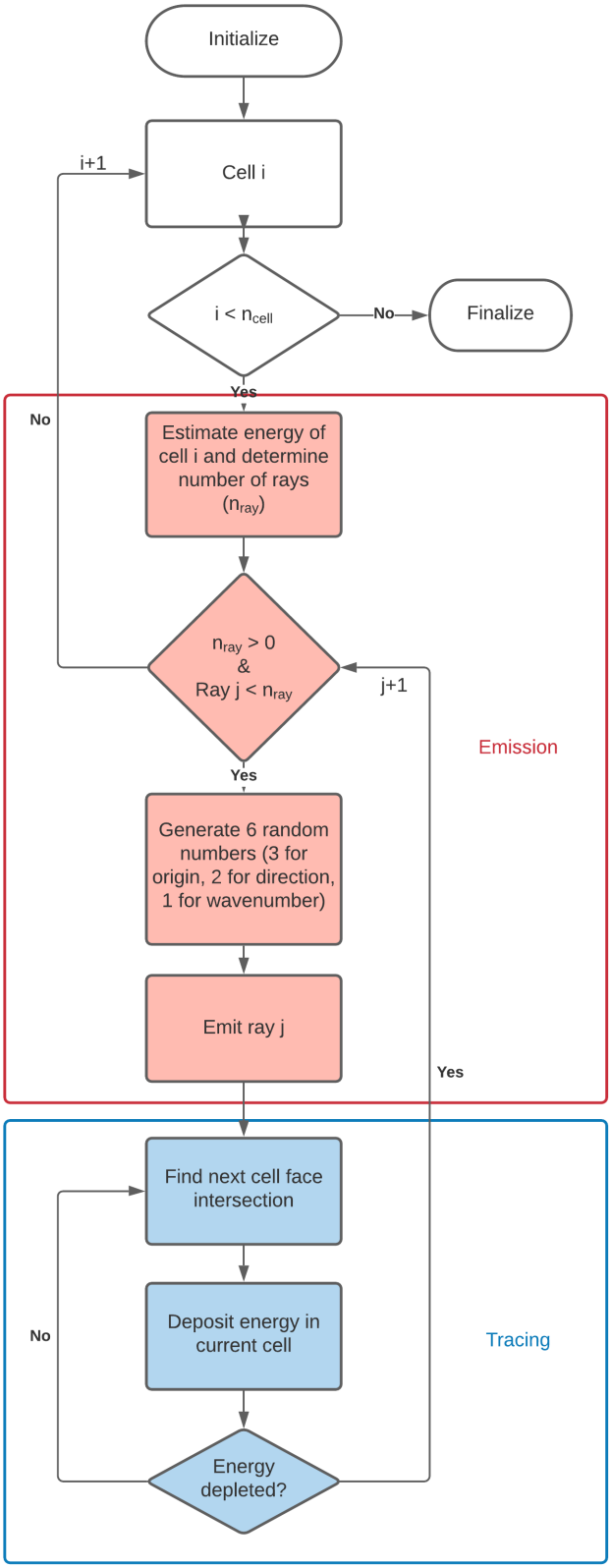

Figure 4.1: Basic flowchart of PMC code modified from [39] with labeled emission and tracing subroutines

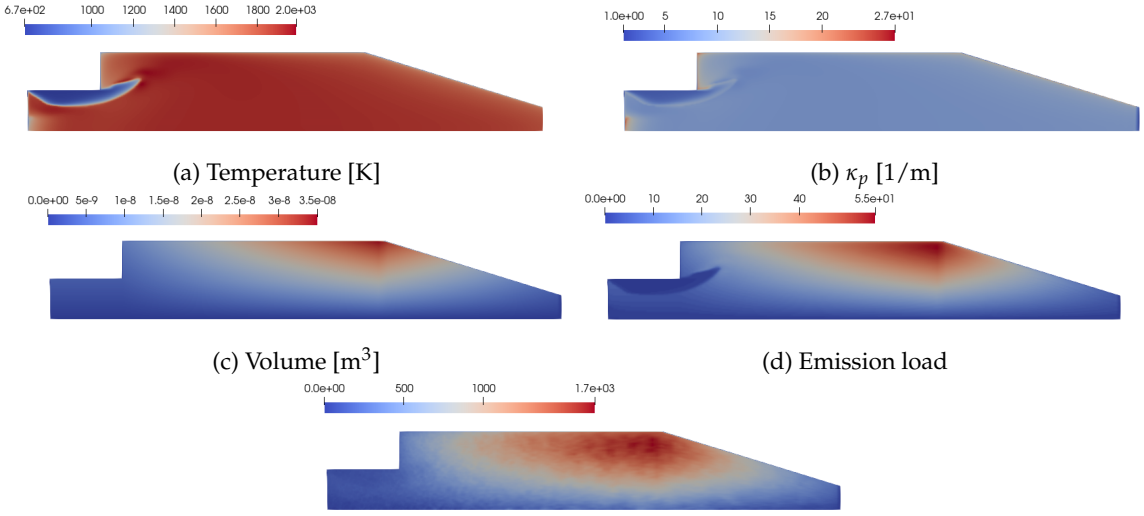

(a) Temperature [K]

(b) κ_p [1/m]

(c) Volume [m^3]

(d) Emission load

(e) Tracing load

Figure 4.2: Contour plots of scalar fields for `gasTurbine`

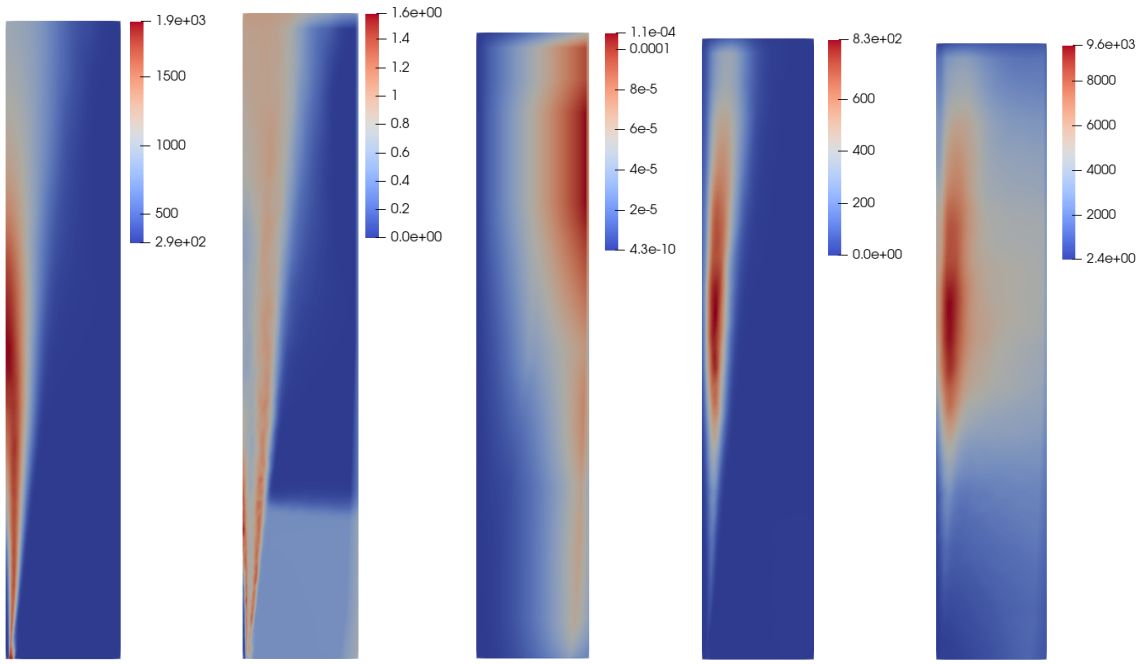

(a) Temperature [K] (b) κ_p [1/m] (c) Volume [m^3] (d) Emission load (e) Tracing load

Figure 4.3: Contour plots of scalar fields for `sandiaDx4`

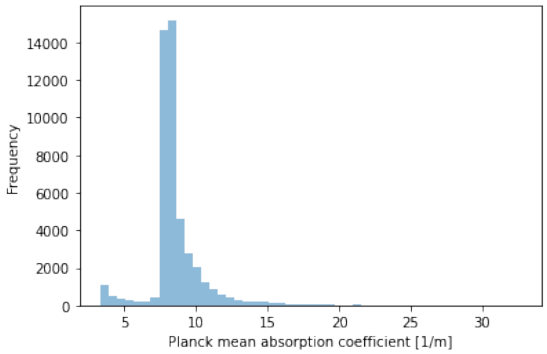

(a) Histogram for Planck-mean absorption coefficient values for `gasTurbine`

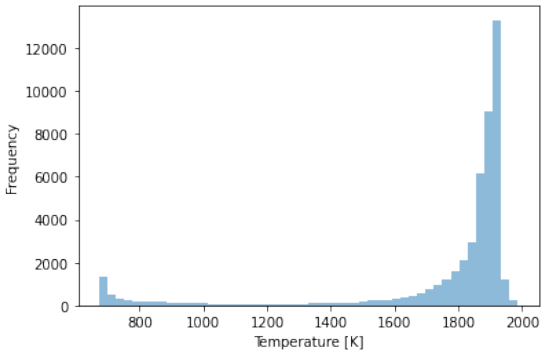

(b) Histogram for temperature values for `gasTurbine`

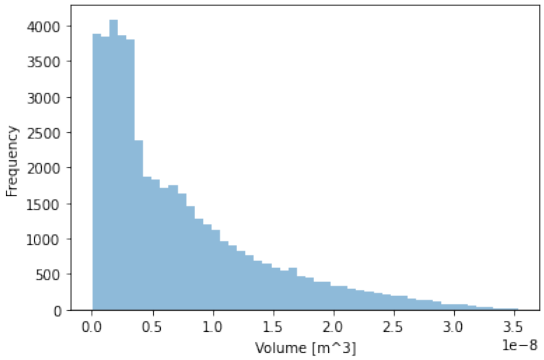

(c) Histogram for volume values for `gasTurbine`

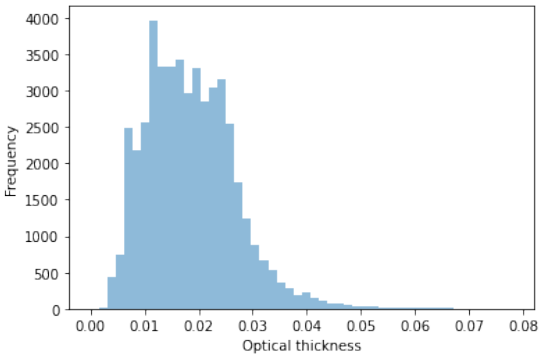

(d) Histogram for optical thickness values for `gasTurbine`

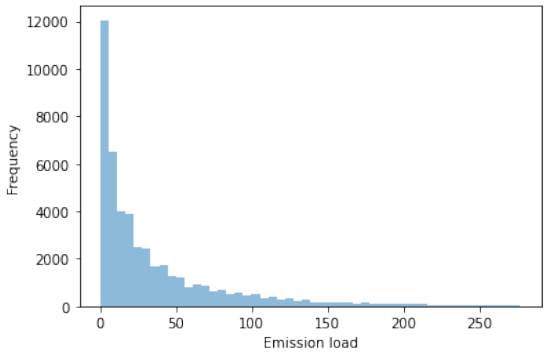

(e) Histogram for emission load values for `gasTurbine`

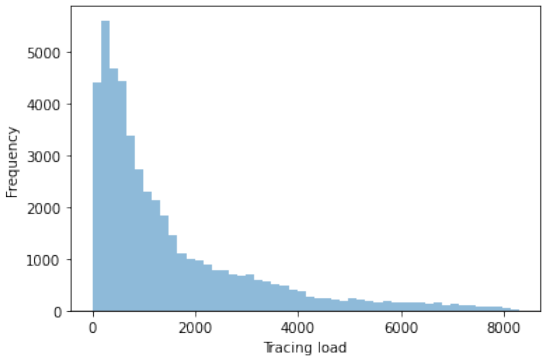

(f) Histogram for tracing load values for `gasTurbine`

Figure 4.4: Histograms for `gasTurbine` data set

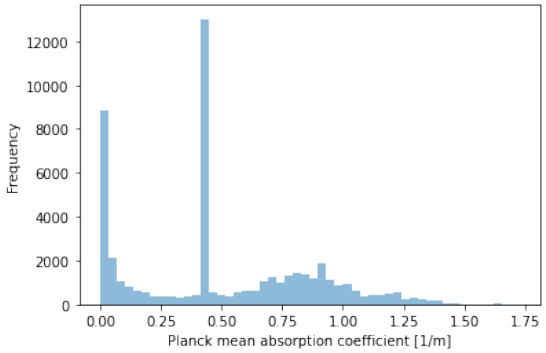

(a) Histogram for Planck-mean absorption coefficient values for `sandiaDx4`

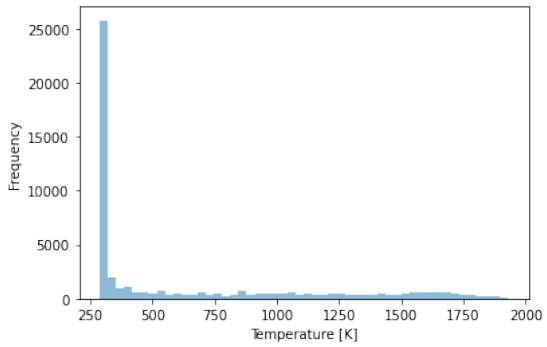

(b) Histogram for temperature values for `sandiaDx4`

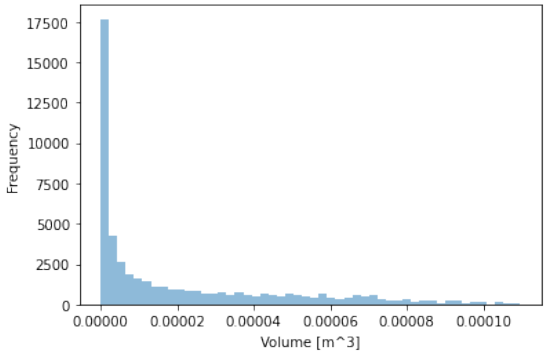

(c) Histogram for volume values for `sandiaDx4`

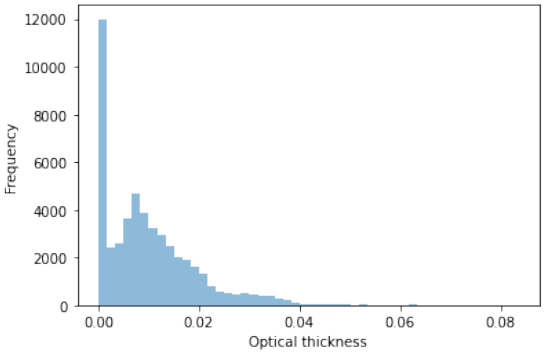

(d) Histogram for optical thickness values for `sandiaDx4`

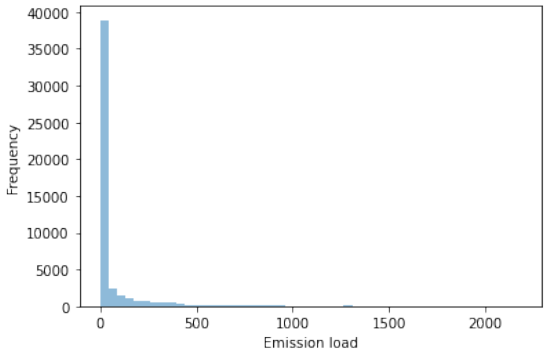

(e) Histogram for emission load values for `sandiaDx4`

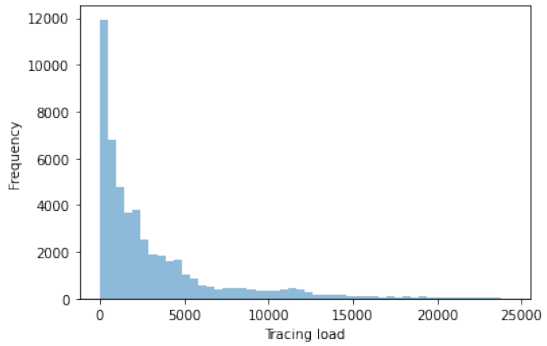

(f) Histogram for tracing load values for `sandiaDx4`

Figure 4.5: Histograms for `sandiaDx4` data set

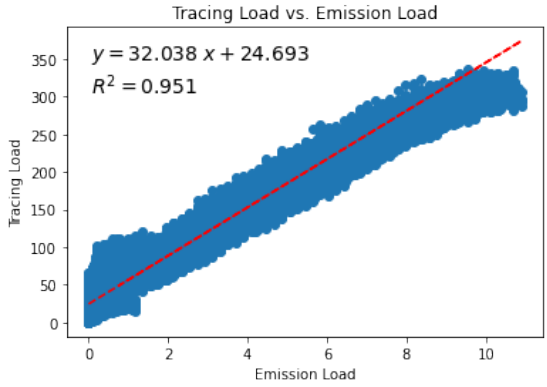

(a) Tracing load vs. emission load (scaled with number of rays and hot cell fraction) for `gasTurbine`

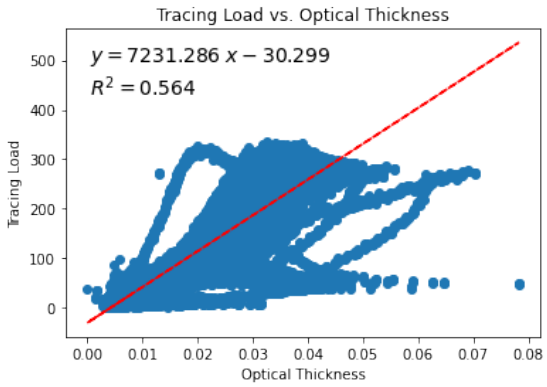

(b) Tracing load (scaled with number of rays and hot cell fraction) vs. optical thickness for `gasTurbine`

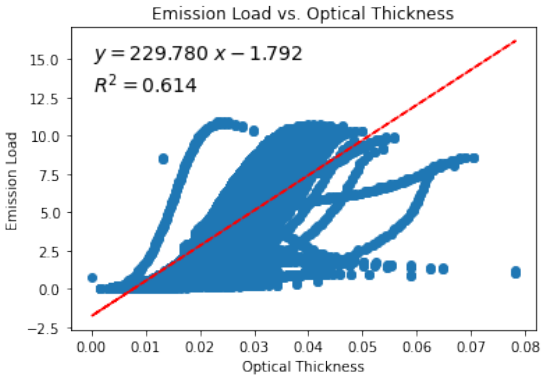

(c) Emission load (scaled with number of rays and hot cell fraction) vs. optical thickness for `gasTurbine`

Figure 4.6: Correlation among various components of emission and tracing load for `gasTurbine`

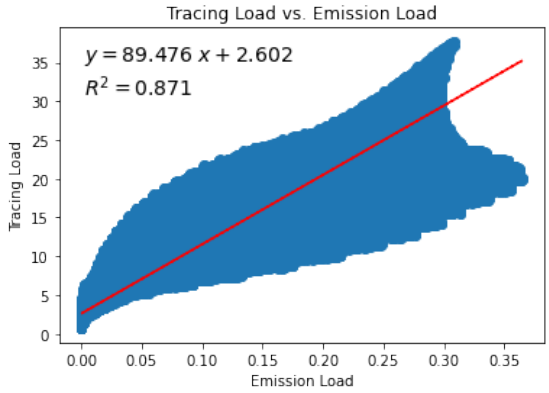

(a) Tracing load vs. emission load (scaled with number of rays and hot cell fraction) for `aachenBomb`

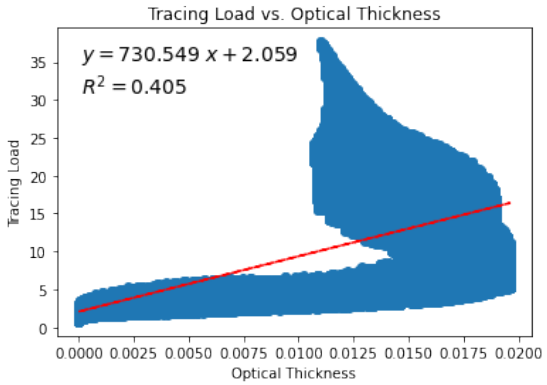

(b) Tracing load (scaled with number of rays and hot cell fraction) vs. optical thickness for `aachenBomb`

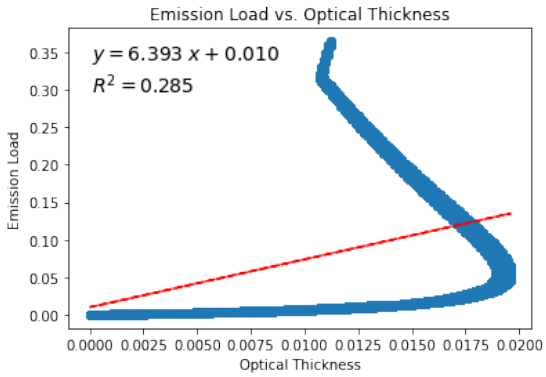

(c) Emission load (scaled with number of rays and hot cell fraction) vs. optical thickness for `aachenBomb`

Figure 4.7: Correlation among various components of emission and tracing load for `aachenBomb`

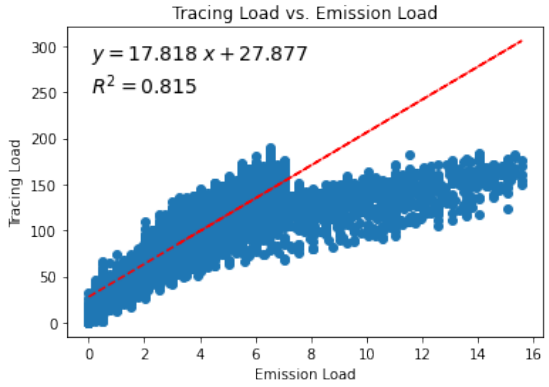

(a) Tracing load vs. emission load (scaled with number of rays and hot cell fraction) for `sprayA`

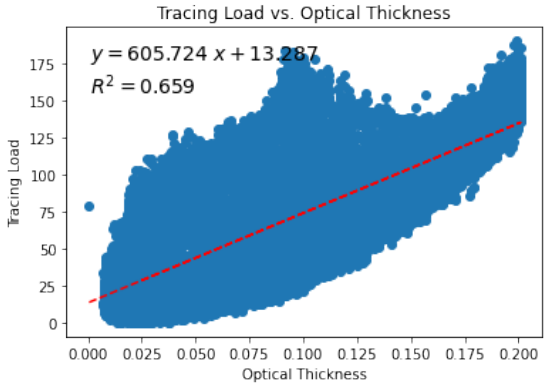

(b) Tracing load (scaled with number of rays and hot cell fraction) vs. optical thickness for `sprayA`

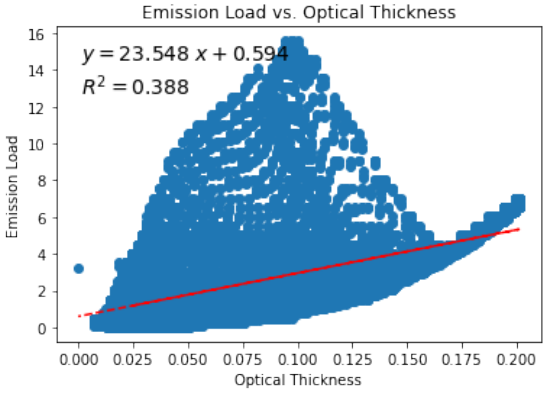

(c) Emission load (scaled with number of rays and hot cell fraction) vs. optical thickness for `sprayA`

Figure 4.8: Correlation among various components of emission and tracing load for `sprayA`

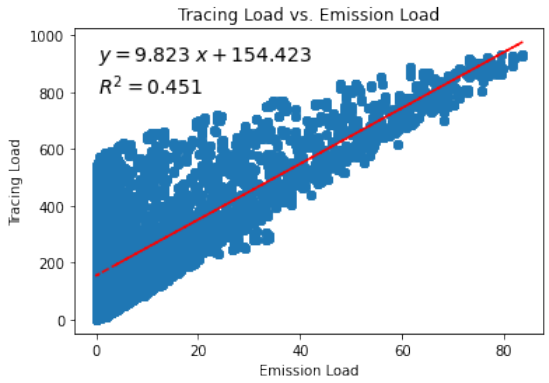

(a) Tracing load vs. emission load (scaled with number of rays and hot cell fraction) for `sandiaDx4`

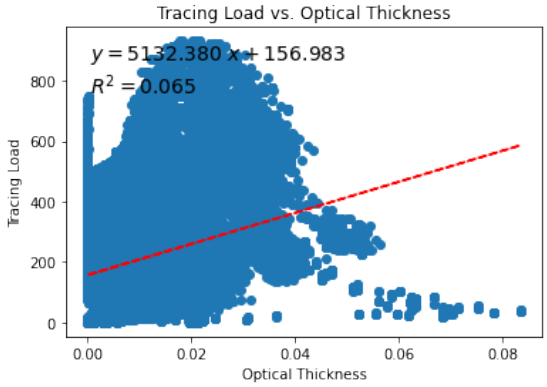

(b) Tracing load (scaled with number of rays and hot cell fraction) vs. optical thickness for `sandiaDx4`

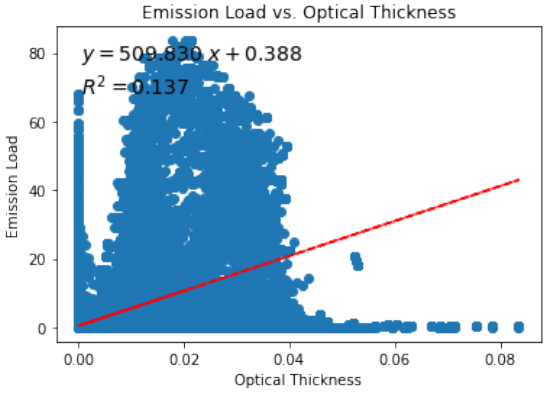

(c) Emission load (scaled with number of rays and hot cell fraction) vs. optical thickness for `sandiaDx4`

Figure 4.9: Correlation among various components of emission and tracing load for `sandiaDx4`

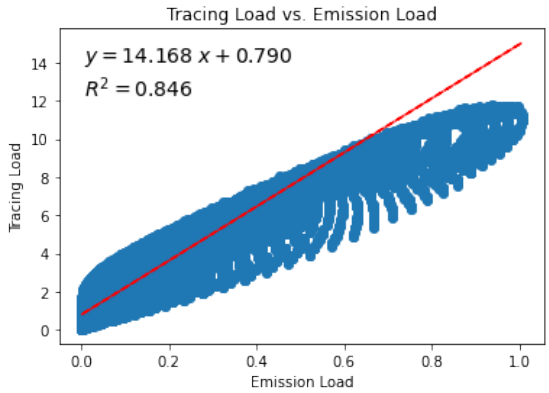

(a) Tracing load vs. emission load (scaled with number of rays and hot cell fraction) for `flameCube`

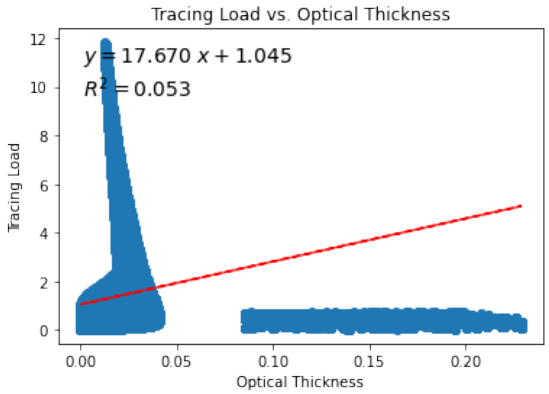

(b) Tracing load (scaled with number of rays and hot cell fraction) vs. optical thickness for `flameCube`

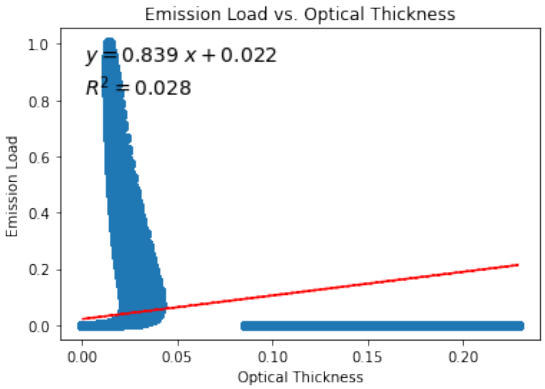

(c) Emission load (scaled with number of rays and hot cell fraction) vs. optical thickness for `flameCube`

Figure 4.10: Correlation among various components of emission and tracing load for `flameCube`

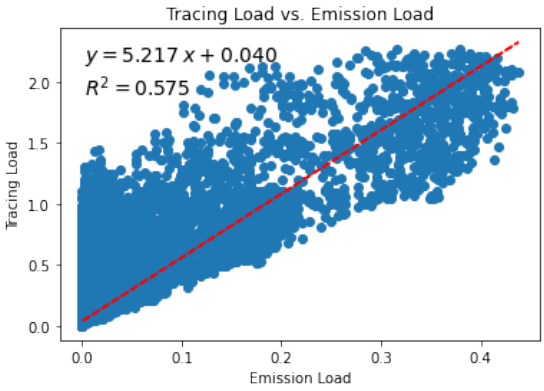

(a) Tracing load vs. emission load (scaled with number of rays and hot cell fraction) for `poolfire2`

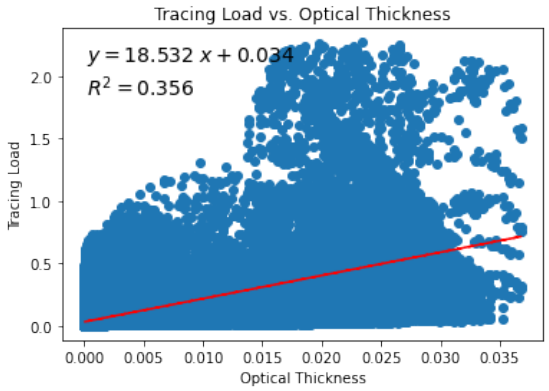

(b) Tracing load (scaled with number of rays and hot cell fraction) vs. optical thickness for `poolfire2`

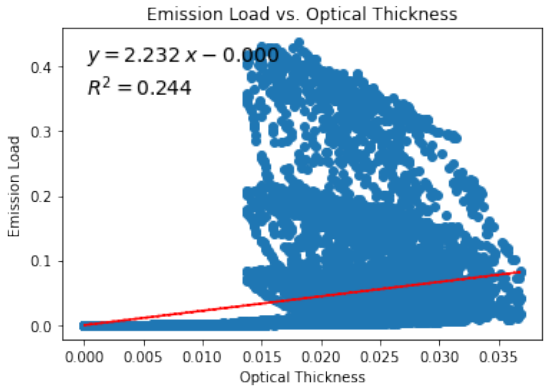

(c) Emission load (scaled with number of rays and hot cell fraction) vs. optical thickness for `poolfire2`

Figure 4.11: Correlation among various components of emission and tracing load for `poolfire2`

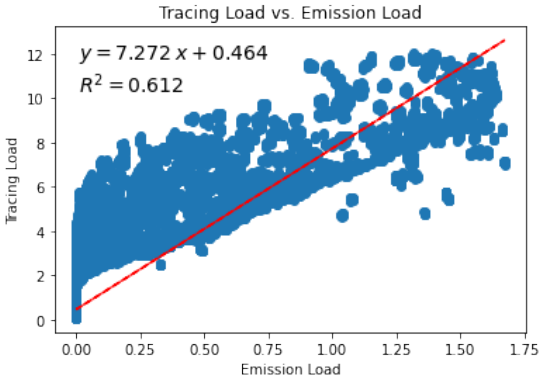

(a) Tracing load vs. emission load (scaled with number of rays and hot cell fraction) for `smallPoolfire3D`

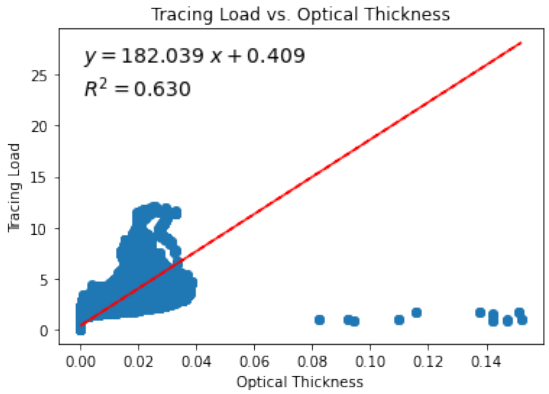

(b) Tracing load (scaled with number of rays and hot cell fraction) vs. optical thickness for `smallPoolfire3D`

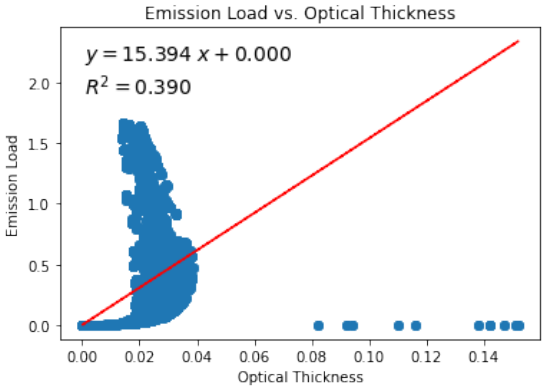

(c) Emission load (scaled with number of rays and hot cell fraction) vs. optical thickness for `smallPoolfire3D`

Figure 4.12: Correlation among various components of emission and tracing load for `smallPoolfire3D`

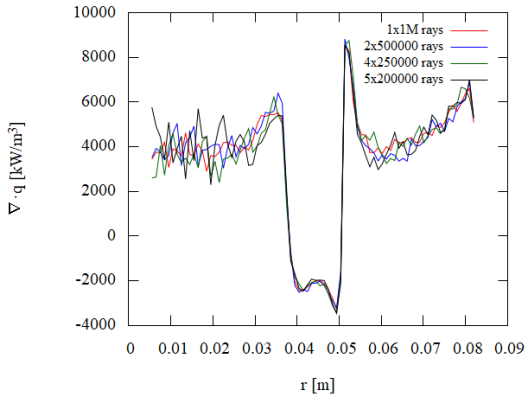

(a) $\nabla \cdot \mathbf{q}$ vs. y (meters)

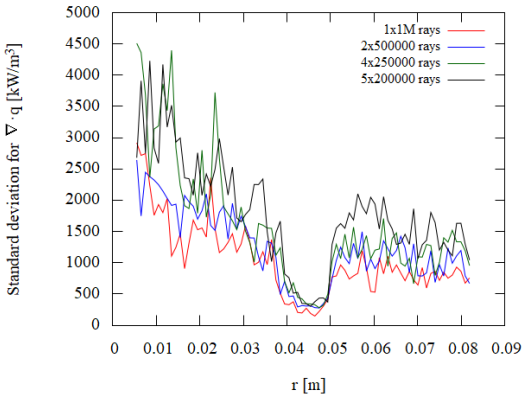

(b) Standard deviation of $\nabla \cdot \mathbf{q}$ vs. y (meters)

Figure 4.13: $\nabla \cdot \mathbf{q}$ and standard deviation for `gasTurbine` at x=0.1 meters

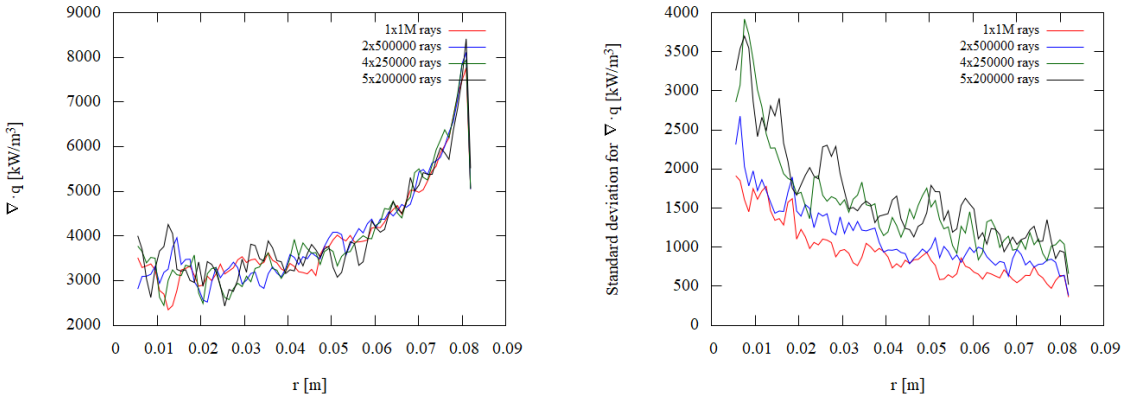

(a) $\nabla \cdot \mathbf{q}$ vs. y (meters) (b) Standard deviation of $\nabla \cdot \mathbf{q}$ vs. y (meters)

Figure 4.14: $\nabla \cdot \mathbf{q}$ and standard deviation for `gasTurbine` at x=0.15 meters

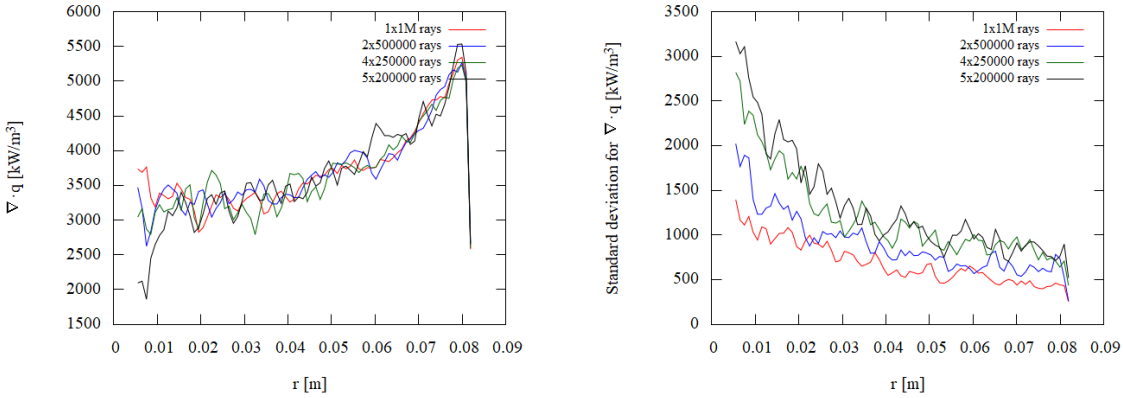

(a) $\nabla \cdot \mathbf{q}$ vs. y (meters) (b) Standard deviation of $\nabla \cdot \mathbf{q}$ vs. y (meters)

Figure 4.15: $\nabla \cdot \mathbf{q}$ and standard deviation for `gasTurbine` at x=0.3 meters

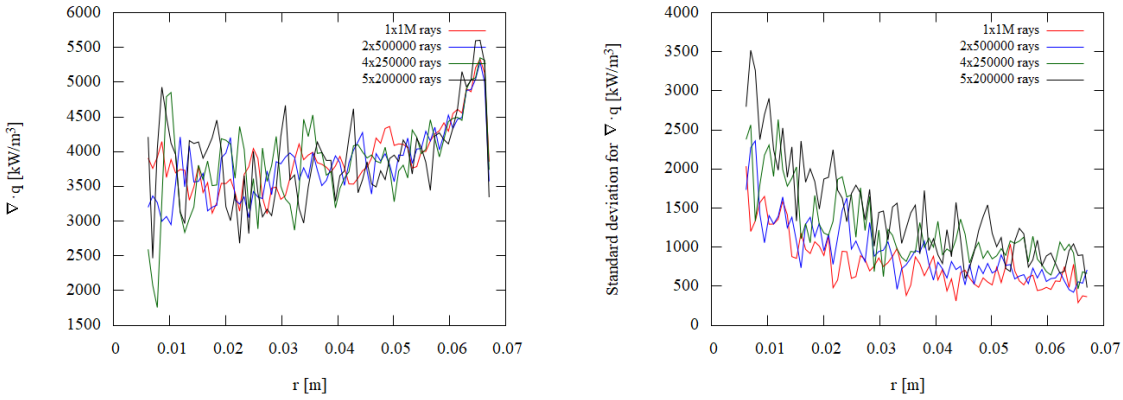

(a) $\nabla \cdot \mathbf{q}$ vs. y (meters) (b) Standard deviation of $\nabla \cdot \mathbf{q}$ vs. y (meters)

Figure 4.16: $\nabla \cdot \mathbf{q}$ and standard deviation for `gasTurbine` at x=0.4 meters

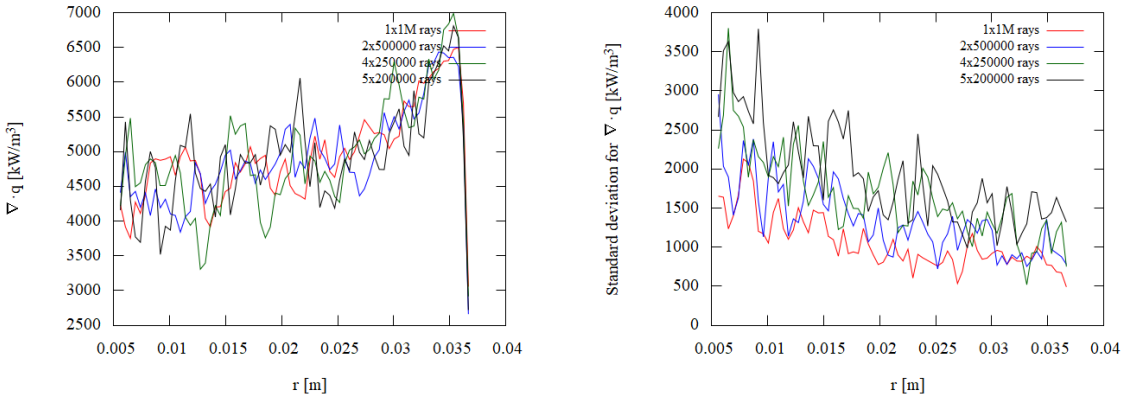

(a) $\nabla \cdot \mathbf{q}$ vs. y (meters) (b) Standard deviation of $\nabla \cdot \mathbf{q}$ vs. y (meters)

Figure 4.17: $\nabla \cdot \mathbf{q}$ and standard deviation for `gasTurbine` at x=0.5 meters

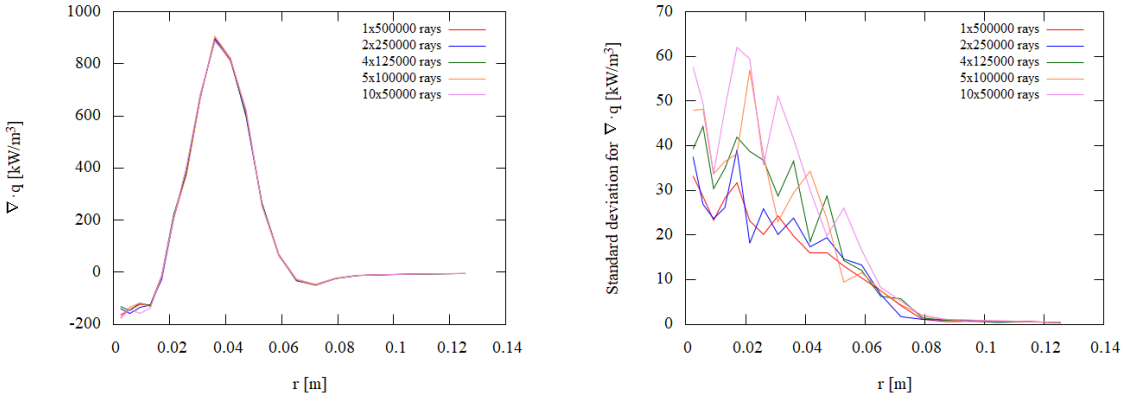

(a) $\nabla \cdot \mathbf{q}$ vs. r (meters) (b) Standard deviation of $\nabla \cdot \mathbf{q}$ vs. r (meters)

Figure 4.18: $\nabla \cdot \mathbf{q}$ and standard deviation for `sandiaDx4` at z/d=14.93

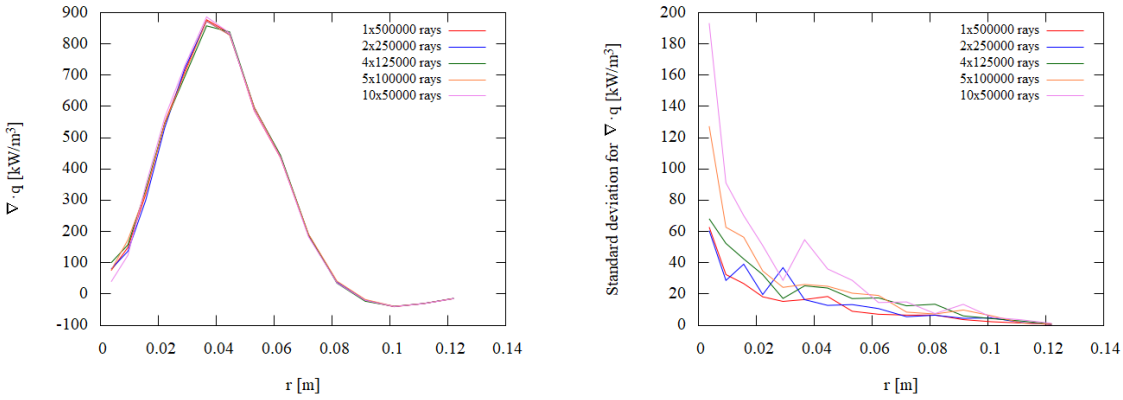

(a) $\nabla \cdot \mathbf{q}$ vs. r (meters) (b) Standard deviation of $\nabla \cdot \mathbf{q}$ vs. r (meters)

Figure 4.19: $\nabla \cdot \mathbf{q}$ and standard deviation for `sandiaDx4` at z/d=29.79

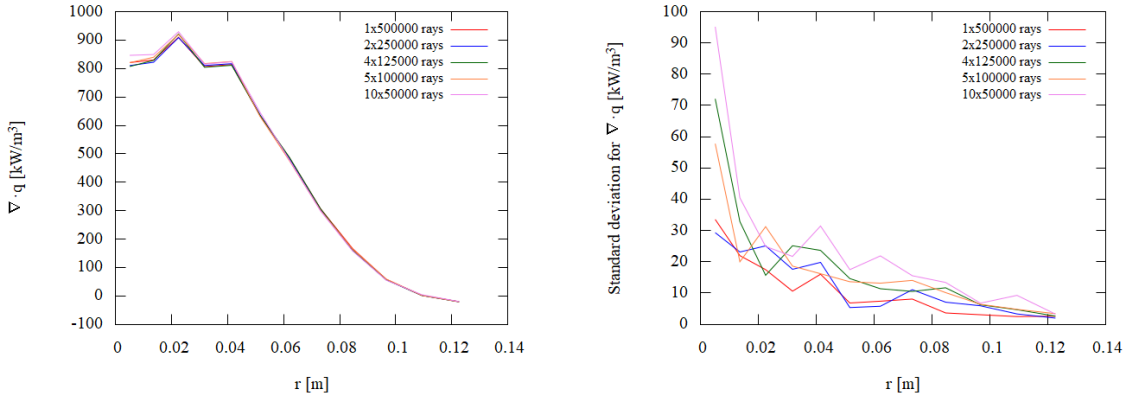

(a) $\nabla \cdot \mathbf{q}$ vs. r (meters) (b) Standard deviation of $\nabla \cdot \mathbf{q}$ vs. r (meters)

Figure 4.20: $\nabla \cdot \mathbf{q}$ and standard deviation for `sandiaDx4` at z/d=44.65

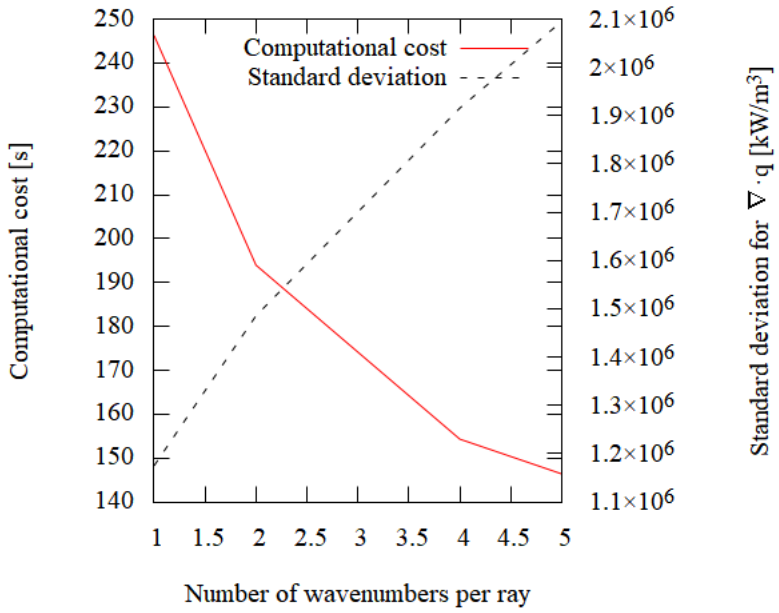

Figure 4.21: Computational cost and standard deviation of $\nabla \cdot \mathbf{q}$ vs. number of wavenumbers per ray for `gasTurbine`

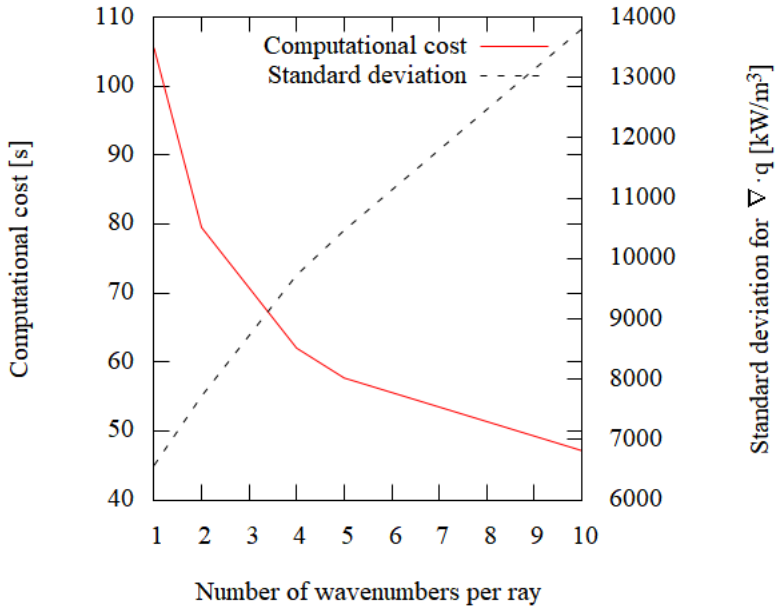

Figure 4.22: Computational cost and standard deviation of $\nabla \cdot \mathbf{q}$ vs. number of wavenumbers per ray for `sandiaDx4`

CHAPTER 5

CONCLUSION

In this work, the three types of RTE solvers are compared in detail. Then, further investigation of potential improvements to the PMC method is conducted.

Overall, the P_N method increased in both accuracy and computational cost with order N. However, the advantage gained in accuracy decreases for each successive increase in N. P_5 and P_7 perform at a similar level of accuracy. The computational cost increased quadratically with order N, which is consistent with the axisymmetric formulation that is used in this work. Finally, SP_3 and SP_5 performed relatively well – at a similar level of accuracy as P_3 and P_5 while exhibiting some savings in computational cost.

In general, the DOM increased in accuracy with the total number of ordinates ($n_\theta \times n_\phi$). However, it was shown that, due to the thin wedge geometry of the problem, discretization in the azimuthal (ϕ) direction had a greater effect on the performance of the RTE solver. Also, computational cost directly correlated to the total number of ordinates used. Thus, different discretization schemes with the same number of total ordinates (e.g. 4×4 and 2×8) required almost equivalent computational cost. From this, the conclusion can be drawn that for the selected configuration, the number of azimuthal ordinates n_ϕ should be increased over the number of polar ordinates n_θ.

The QMC method also retains a high level of accuracy for a smaller number of rays than the PMC method. For most locations, the value for $\nabla \cdot \mathbf{q}$ calculated by QMC fell within the standard error of PMC LBL calculations.

When one P_N RTE solver and one DOM solver that require an approximately equal computational cost are compared with QMC results, the DOM RTE solver is shown to perform better than P_N. However, QMC still performs better compared to both P_N and DOM at half the computational cost. Thus, for the chosen configuration, QMC performs the best, followed by DOM. However, this conclusion can only be drawn for the specific implementation of RTE solvers that is used in this work. A major limitation of this study is that the computational cost is affected by more than just the RTE solver. For example, the differential equation solvers that are used by OpenFOAM can be tuned for a maximum number of iterations or a desired tolerance. Thus, these comparisons are qualitative only.

Two primary improvements to the PMC method are suggested: an a priori estimation of computational load using local variables and a feature to trace multiple wavenumbers per ray, deemed "ray bundling." Qualitatively, the a priori estimation results show a noticeable correlation between the tracing load and the emission load, which can be calculated directly from the volume, temperature, and Planck mean absorption coefficient. However, a linear regression analysis of the relation between tracing load and emission load show that the correlation between these two variables is only good for high-pressure cases and for artificial case `flameCube`. The relationship between tracing load and optical thickness is also investigated, but the results suggest that there is little to no correlation between these two variables. Hence, it can be concluded that a good correlation between emission load and tracing load can be drawn for high-pressure cases. Thus, local values for temperature, volume, and Planck mean absorption coefficient can be used to estimate the computational load distribution of a PMC calculation before it is conducted. This opens the potential to distribute the computational load evenly between processors in parallel Monte Carlo calculations. For atmospheric pressure cases, further investigation is required before a suitable correlation can be formed.

Tracing multiple wavenumbers per ray is shown to increase the statistical error and decrease the computational cost of PMC calculations. Thus, optimized values for the number of wavenumbers per ray for the `gasTurbine` and `sandiaDx4` cases are found. These results can also be used to tune the number of wavenumbers per ray for a specific application.

CHAPTER 6

FUTURE WORK

6.1 Parallelization in the Wavenumber Domain

In [47], O'brien et al describe two primary methods of parallelizing Monte Carlo particle transport calculations, spatial parallelism and particle parallelism. These are illustrated in Figure 6.1. Spatial parallelism is the parallelization method where the computational domain is decomposed and each subdomain is assigned to a single processor. In Figure 6.1, spatial parallelism is illustrated by using subdomains of different colors. Particle parallelism instead assigns a specific number of particles or rays to each processor. Each processor stores a copy of the entire computational domain and proceeds to emit and trace all the particles that are assigned to it. In Figure 6.1, two copies of the domain are seen, and an equal number of rays are traced separately on each copy of the domain, indicating that each subset of rays would be traced across the entire domain by a single processor. This method of parallelization may not be feasible for extremely large computational domains such that a copy of the domain exceeds the memory of a single processor. Nonetheless, its parallel efficiency is significantly higher than that of spatial parallelism. Communication between processors is only required once after all particles have been traced, and the computational load is more balanced across all processors.

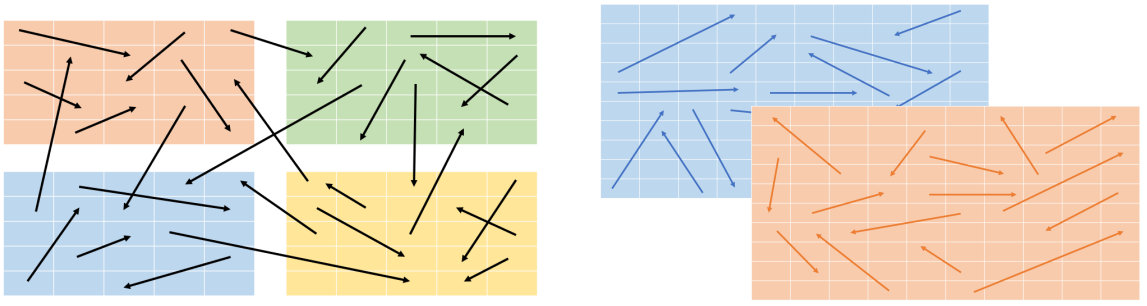

(a) Spatial parallelism (i.e. domain decomposition)

(b) Particle parallelism (i.e. domain replication)

Figure 6.1: Illustration of two methods of Monte Carlo parallelization motivated by [47]

Particle parallelism could be implemented in radiation Monte Carlo calculations by dividing the computational load based on wavenumber η. For example, wavenumbers $\eta \in [\eta_i, \eta_{i+1}]$ could be assigned to processor i, and so on. For smaller combustion simulations that

do not require a large portion of memory, the option to parallelize by wavenumber could speed up PMC calculations immensely. Since the PMC code in this work is implemented on the CFD software OpenFOAM, it may be necessary to create a separate mesh for radiation calculations. Still, the efficiency advantage of particle parallelism is significant.

6.2 Dynamic Load Balancing of Monte Carlo Calculations

O'Brien et al also detail a new implementation of dynamic load balancing in Monte Carlo particle transport calculations in [48], building on the previous work in [47]. For calculations where the entire computational domain cannot be stored by a single processors, this may be a valuable avenue of exploration. Dynamic load balancing combines spatial parallelism and particle parallelism by dividing the domain into subdomains and assigning multiple processors to a single subdomain. For subdomains of high particle density and thus high predicted computational load, more processors are allocated, and vice versa. This uneven distribution among subdomains balances the computational load between processors. Furthermore, as the computational load changes from one timestep to the next, the allocation of processors to each subdomain also changes.

The load balancing algorithm in [47] requires each processor to have knowledge of the computational load across the entire domain in order to balance the load. As the number of processors gets extremely large, the load balancing step can surprisingly take more time than the Monte Carlo calculation itself. However, the algorithm in [48] requires each processor to only know the predicted computational load of its "neighbor." For more and more processors, the efficiency of this load balancing algorithm exceeds the efficiency of the other. Implementation of both of these load balancing algorithms would be an improvement to the current Monte Carlo solver used in radiation calculations in this work, which does not feature any load-balancing option.

6.3 Improved Correlation between Local Variables and Tracing Load for Atmospheric Pressure Cases

A primary limitation of this work is that a sufficient correlation between local variables (e.g. temperature) and the tracing load for all atmospheric pressure cases could not be developed. There are a few avenues that are worth more exploration. First, there is the possibility of redefining the optical thickness of each cell using the mean beam length as the length scale instead

of the diameter of a sphere of equivalent volume. An approximate equation for the mean beam length L_m for a generic volume V with surface area A is given by [18]

$$L_m = 3.6\frac{V}{A}. \tag{6.1}$$

This could potentially provide a more accurate measure of the average distance that a ray travels when passing through a finite volume cell, and since face area and volume information is available through OpenFOAM, this is a natural next step in the search for a meaningful correlation between tracing load and local variables. Other local variables that were not included in the analysis in this work are species mass fractions, which could affect the computational load distribution and should therefore be investigated in future work.

BIBLIOGRAPHY

[1] Zhu, X. L., & Gore, J. P. (2005). Radiation effects on combustion and pollutant emissions of high-pressure opposed flow methane/air diffusion flames. Combustion and Flame, 141(1–2), 118–130. https://doi.org/10.1016/j.combustflame.2004.12.012

[2] Liu, F., Guo, H., & Smallwood, G. J. (2004). Effects of radiation model on the modeling of a laminar coflow methane/air diffusion flame. Combustion and Flame, 138(1–2), 136–154. https://doi.org/10.1016/j.combustflame.2004.04.007

[3] Liu, F., Smallwood, G. J., & Kong, W. (2011). The importance of thermal radiation transfer in laminar diffusion flames at normal and microgravity. Journal of Quantitative Spectroscopy and Radiative Transfer, 112(7), 1241–1249. https://doi.org/10.1016/j.jqsrt.2010.08.021

[4] Moussa, R. Ben, Guessasma, M., Proust, C., Saleh, K., & Fortin, J. (2015). Thermal radiation contribution to metal dust explosions. Procedia Engineering, 102, 714–721. https://doi.org/10.1016/j.proeng.2015.01.172

[5] Liu, F., Guo, H., Smallwood, G. J., & El Hafi, M. (2004). Effects of gas and soot radiation on soot formation in counterflow ethylene diffusion flames. Journal of Quantitative Spectroscopy and Radiative Transfer, 84(4), 501–511. https://doi.org/10.1016/S0022-4073(03)00267-X

[6] Schoegl, I. (2012). Radiation effects on flame stabilization on flat flame burners. Combustion and Flame, 159(9), 2817–2828. https://doi.org/10.1016/j.combustflame.2012.05.010

[7] Bidi, M., Hosseini, R., & Nobari, M. R. H. (2008). Numerical analysis of methane-air combustion considering radiation effect. Energy Conversion and Management, 49(12), 3634–3647. https://doi.org/10.1016/j.enconman.2008.07.010

[8] Poitou, D., Amaya, J., El Hafi, M., & Cuénot, B. (2012). Analysis of the interaction between turbulent combustion and thermal radiation using unsteady coupled LES/DOM simulations. Combustion and Flame, 159(4), 1605–1618. https://doi.org/10.1016/j.combustflame.2011.12.016

[9] Yin, C., Rosendahl, L. A., & Kær, S. K. (2011). Chemistry and radiation in oxy-fuel combustion: A computational fluid dynamics modeling study. Fuel, 90(7), 2519–2529. https://doi.org/10.1016/j.fuel.2011.03.023

[10] Tkachenko, S., Timchenko, V., Yeoh, G., & Reizes, J. (2019). Effects of radiation on turbulent natural convection in channel flows. International Journal of Heat and Fluid Flow, 77(August 2018), 122–133. https://doi.org/10.1016/j.ijheatfluidflow.2019.03.009

[11] Deshmukh, K. V., Modest, M. F., & Haworth, D. C. (2008). Direct numerical simulation of turbulence-radiation interactions in a statistically one-dimensional nonpremixed system. Journal of Quantitative Spectroscopy and Radiative Transfer, 109(14), 2391–2400. https://doi.org/10.1016/j.jqsrt.2008.04.005

[12] Gupta, A., Modest, M. F., & Haworth, D. C. (2009). Large-eddy simulation of turbulence-radiation interactions in a turbulent planar channel flow. Journal of Heat Transfer, 131(6), 1–8. https://doi.org/10.1115/1.3085875

[13] Deshmukh, K. V., Modest, M. F., & Haworth, D. C. (2009). Higher-order spherical harmonics to model radiation in direct numerical simulation of turbulent reacting flows. Computational Thermal Sciences, 1(2), 207–230. https://doi.org/10.1615/ComputThermalScien.v1.i2.60

[14] Yoshikawa, T., & Reitz, R. D. (2009). Effect of radiation on diesel engine combustion and heat transfer. Journal of Thermal Science and Technology, 4(1), 86–97. https://doi.org/10.1299/jtst.4.86

[15] Naraghi, M., Dunn, S., & Coats, D. (2005). Modeling of Radiation Heat Transfer in Liquid Rocket Engines. July. https://doi.org/10.2514/6.2005-3935

[16] Goebel, F., Kniesner, B., Frey, M., Knab, O., & Mundt, C. (2014). Radiative heat transfer analysis in modern rocket combustion chambers. CEAS Space Journal, 6(2), 79–98. https://doi.org/10.1007/s12567-014-0060-2

[17] Modest, M. F., & Haworth, D. C. (2015). Radiative Heat Transfer in Turbulent Combustion Systems. Springer.

[18] Modest, M. F. (2013). Radiative Heat Transfer (3rd ed.). Academic Press.

[19] Cai, J., Roy, S., & Modest, M. F. (2016). A comparison of specularly reflective boundary conditions and rotationally invariant formulations for Discrete Ordinate Methods in axisymmetric geometries. Journal of Quantitative Spectroscopy and Radiative Transfer, 182, 75–86. https://doi.org/10.1016/j.jqsrt.2016.05.005

[20] Modest, M. F., & Yang, J. (2008). Elliptic PDE formulation and boundary conditions of the spherical harmonics method of arbitrary order for general three-dimensional geometries. Journal of Quantitative Spectroscopy and Radiative Transfer, 109(9), 1641–1666. https://doi.org/10.1016/j.jqsrt.2007.12.018

[21] Ge, W. (2017). High-Order Spherical Harmonics Methods for Radiative Heat Transfer and Applications in Combustion Simulations. https://cloudfront.escholarship.org/dist/prd/content/qt2g85768d/qt2g85768d.pdf?t=osfbe9

[22] Ge, W., Modest, M. F., & Marquez, R. (2015). Two-dimensional axisymmetric formulation of high order spherical harmonics methods for radiative heat transfer. Journal of Quantitative Spectroscopy and Radiative Transfer, 156, 58–66. https://doi.org/10.1016/j.jqsrt.2015.01.013

[23] Modest, M. F. (2012). Further Development of the Elliptic PDE Formulation of the P N Approximation and its Marshak Boundary Conditions. Numerical Heat Transfer, Part B: Fundamentals, 62(2–3), 181–202. https://doi.org/10.1080/10407790.2012.702645

[24] Nocedal, J., & Wright, S. J. (2006). Numerical Optimization (2nd ed.). Springer Science+Business Media, LLC.

[25] Modest, M. F., Cai, J., Ge, W., & Lee, E. (2014). Elliptic formulation of the Simplified Spherical Harmonics Method in radiative heat transfer. International Journal of Heat and Mass Transfer, 76, 459–466. https://doi.org/10.1016/j.ijheatmasstransfer.2014.04.038

[26] Farmer, J., & Roy, S. (2020). A quasi-Monte Carlo solver for thermal radiation in participating media: A QMC solver for thermal radiation in participating media. Journal of Quantitative

Spectroscopy and Radiative Transfer, 242, 106753.
https://doi.org/10.1016/j.jqsrt.2019.106753

[27] Rothman, L. S., Gordon, I. E., Barbe, A., Benner, D. C., Bernath, P. F., Birk, M., Boudon, V., Brown, L. R., Campargue, A., Champion, J. P., Chance, K., Coudert, L. H., Dana, V., Devi, V. M., Fally, S., Flaud, J. M., Gamache, R. R., Goldman, A., Jacquemart, D., … Vander Auwera, J. (2009). The HITRAN 2008 molecular spectroscopic database. Journal of Quantitative Spectroscopy and Radiative Transfer, 110(9–10), 533–572.
https://doi.org/10.1016/j.jqsrt.2009.02.013

[28] Rothman, L. S., Gordon, I. E., Barber, R. J., Dothe, H., Gamache, R. R., Goldman, A., Perevalov, V. I., Tashkun, S. A., & Tennyson, J. (2010). HITEMP, the high-temperature molecular spectroscopic database. Journal of Quantitative Spectroscopy and Radiative Transfer, 111(15), 2139–2150. https://doi.org/10.1016/j.jqsrt.2010.05.001

[29] Ren, T., & Modest, M. F. (2013). A hybrid wavenumber selection scheme for line-by-line photon Monte Carlo simulations in high- temperature gases. Journal of Heat Transfer, 135(8), 1–4. https://doi.org/10.1115/1.4024385

[30] Wang, C., Ge, W., Modest, M. F., & He, B. (2016). A full-spectrum k-distribution look-up table for radiative transfer in nonhomogeneous gaseous media. Journal of Quantitative Spectroscopy and Radiative Transfer, 168, 46–56. https://doi.org/10.1016/j.jqsrt.2015.08.017

[31] Barlow, R. S., Frank, J. H., Karpetis, A. N., & Chen, J. Y. (2005). Piloted methane/air jet flames: Transport effects and aspects of scalar structure. Combustion and Flame, 143(4), 433–449.
https://doi.org/10.1016/j.combustflame.2005.08.017

[32] Ge, W., David, C., Roy, S., Modest, M., & Ramanan, S. (2021). Comparison of Spherical Harmonics Method and Discrete Ordinates Method for Radiative Transfer in a Turbulent Jet Flame. Journal of Quantitative Spectroscopy and Radiative Transfer. Manuscript in progress.

[33] Pal, G., Gupta, A., Modest, M. F., & Haworth, D. C. (2015). Comparison of accuracy and computational expense of radiation models in simulation of non-premixed turbulent jet flames. Combustion and Flame, 162(6), 2487–2495.
https://doi.org/10.1016/j.combustflame.2015.02.017

[34] Cai, J., Marquez, R., & Modest, M. F. (2014). Comparisons of radiative heat transfer calculations in a jet diffusion flame using spherical harmonics and k-Distributions. Journal of Heat Transfer, 136(11), 1–9. https://doi.org/10.1115/1.4026169

[35] Mazumder, S. (2019). Application of a variance reduction technique to Surface-to-Surface Monte Carlo radiation exchange calculations. International Journal of Heat and Mass Transfer, 131, 424–431. https://doi.org/10.1016/j.ijheatmasstransfer.2018.11.050

[36] Davis, A., & Turner, A. (2011). Comparison of global variance reduction techniques for Monte Carlo radiation transport simulations of ITER. Fusion Engineering and Design, 86(9–11), 2698–2700. https://doi.org/10.1016/j.fusengdes.2011.01.059

[37] OpenFOAM. (n.d.). https://www.openfoam.com/

[38] Fleck, J. A., & Canfield, E. H. (1984). A random walk procedure for improving the computational efficiency of the implicit Monte Carlo method for nonlinear radiation

transport. Journal of Computational Physics, 54(3), 508–523. https://doi.org/10.1016/0021-9991(84)90130-X

[39] Farmer, J. (2019). Development of a Quasi-Monte Carlo Method for Thermal Radiation.

[40] Klassen, M., & Gore, J. P. (1994). Structure and radiation properties of pool fires (p. 153). NIST.

[41] Wu, B., Roy, S. P., & Zhao, X. (2020). Detailed modeling of a small-scale turbulent pool fire. Combustion and Flame, 214, 224–237. https://doi.org/10.1016/j.combustflame.2019.12.034

[42] Roy, S. P. Personal Communication (2021).

[43] SGT-100. (n.d.). https://www.siemens-energy.com/global/en/offerings/power-generation/gas-turbines/sgt-100.html

[44] Ren, T., Modest, M. F., & Roy, S. (2018). Monte carlo simulation for radiative transfer in a high-pressure industrial gas turbine combustion chamber. Journal of Engineering for Gas Turbines and Power, 140(5), 1–10. https://doi.org/10.1115/1.4038153

[45] Pickett, L. M., Genzale, C. L., Bruneaux, G., Malbec, L.-M., Hermant, L., Christiansen, C., & Schramm, J. (2010). Comparison of Diesel Spray Combustion in Different High-Temperature, High-Pressure Facilities. SAE International Journal of Engines, 3(2), 2010-01–2106. https://doi.org/10.4271/2010-01-2106

[46] Mukut, K. M., & Roy, S. P. (2018). A Sensitivity Study on Soot and NOx Formation in High Pressure Combustion System. 2018 Spring Technical Meeting of Central States Section of the Combustion Institute, May.

[47] O'Brien, M., Taylor, J., & Procassini, R. (2005). Dynamic load balancing of parallel Monte Carlo transport calculations. Monte Carlo 2005 Topical Meeting, 1461–1473.

[48] O'Brien, M. J., Brantley, P. S., & Joy, K. I. (2013). Scalable load balancing for massively parallel distributed Monte Carlo particle transport. International Conference on Mathematics and Computational Methods Applied to Nuclear Science and Engineering, M and C 2013, 1(May 2013), 647–658. https://doi.org/10.13140/2.1.5121.6967

APPENDIX A

QUALITITATIVE LOAD DISTRIBUTION DATA

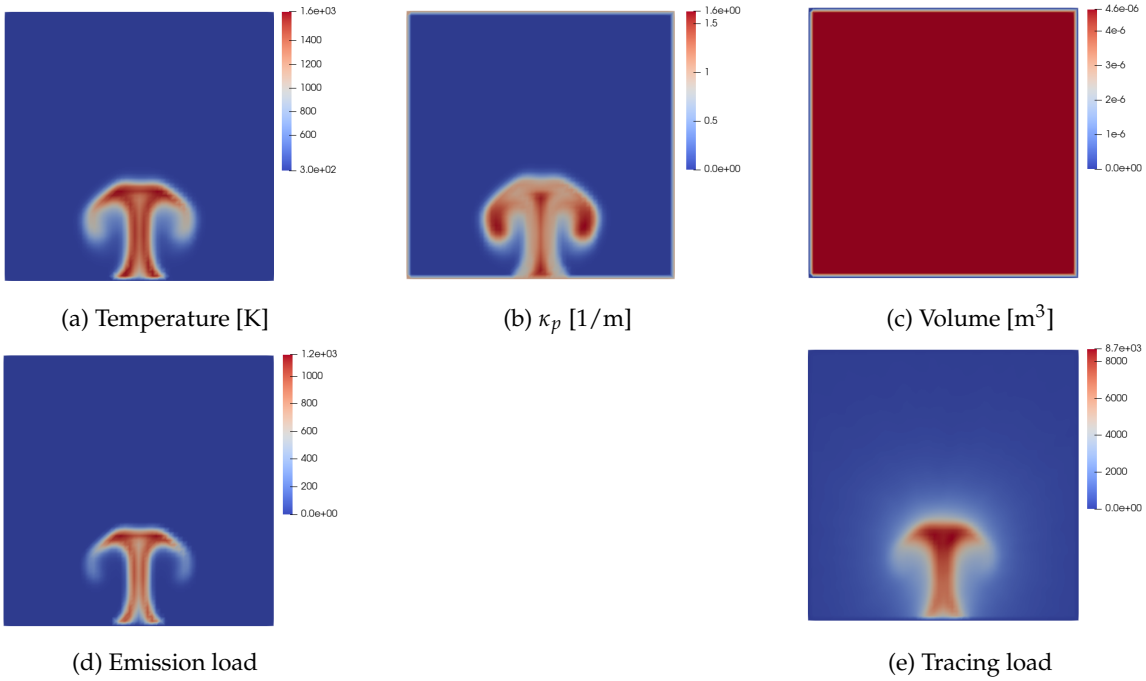

(a) Temperature [K] (b) κ_p [1/m] (c) Volume [m^3]

(d) Emission load (e) Tracing load

Figure A.1: Contour plots of scalar fields for `smallPoolfire3D`

Table A.1: Correlation coefficient data for `smallPoolfire3D`

Relation Variables	Correlation Coefficient)
Emission Load - Optical Thickness	0.5384
Emission Load - kPlanck	0.5384
Emission Load - Temperature	0.7940
Emission Load - Volume	N/A
Tracing Load - Optical Thickness	0.6612
Tracing Load - kPlanck	0.6612
Tracing Load - Temperature	0.7382
Tracing Load - Volume	N/A
Tracing Load - Emission Load	0.7680

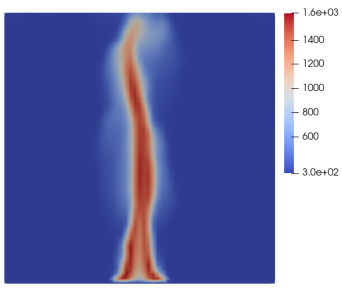

(a) Temperature [K]

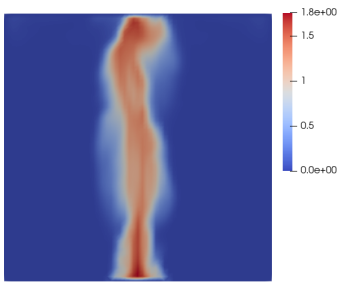

(b) κ_p [1/m]

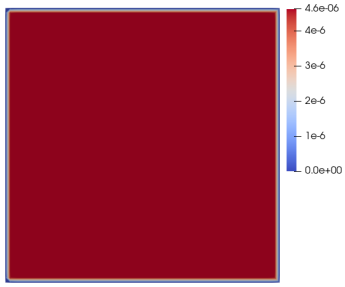

(c) Volume [m^3]

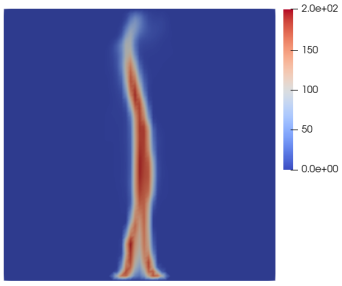

(d) Emission load

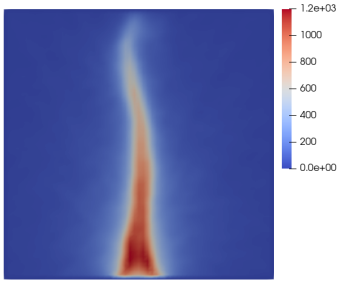

(e) Tracing load

Figure A.2: Contour plots of scalar fields for `poolfire2`

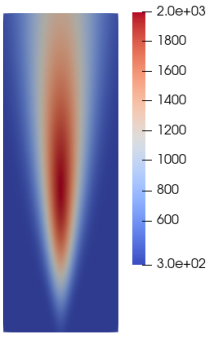

(a) Temperature [K]

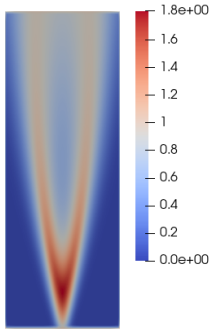

(b) κ_p [1/m]

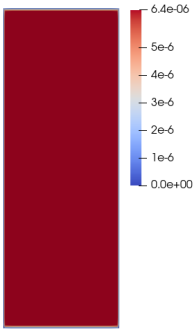

(c) Volume [m^3]

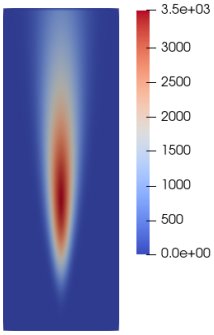

(d) Emission load

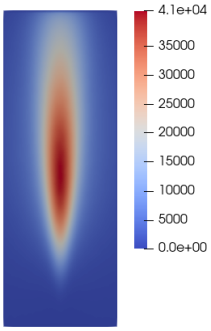

(e) Tracing load

Figure A.3: Contour plots of scalar fields for `flameCube`

Table A.2: Correlation coefficient data for `smallPoolfire`

Relation Variables	Correlation Coefficient
Emission Load - Optical Thickness	0.5724
Emission Load - kPlanck	0.5724
Emission Load - Temperature	0.9128
Emission Load - Volume	N/A
Tracing Load - Optical Thickness	0.7172
Tracing Load - kPlanck	0.7172
Tracing Load - Temperature	0.8525
Tracing Load - Volume	N/A
Tracing Load - Emission Load	0.7771

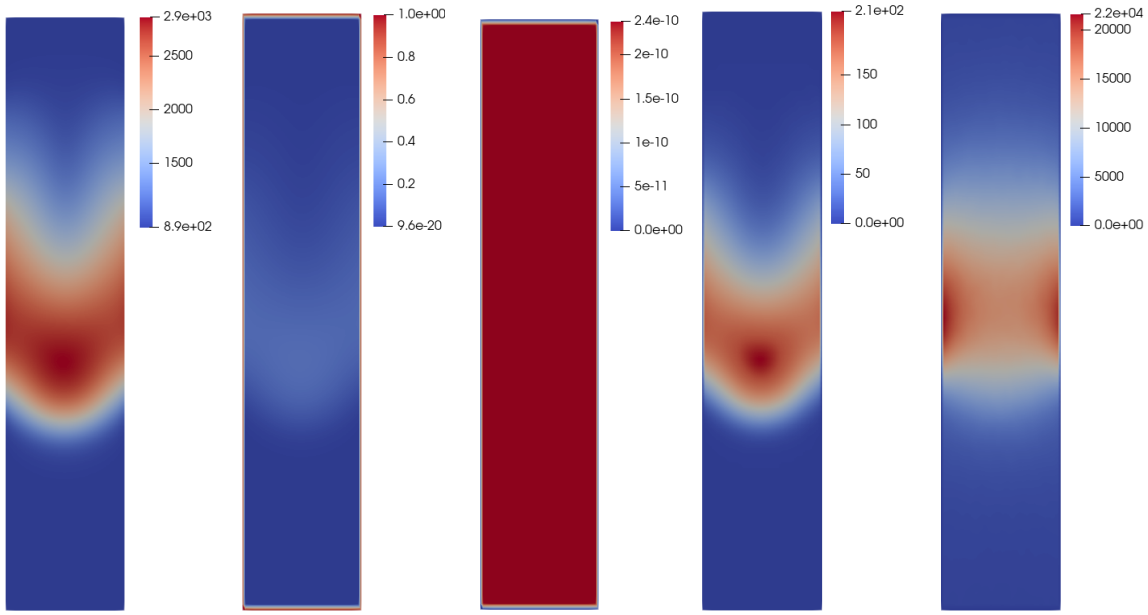

(a) Temperature [K] (b) κ_p [1/m] (c) Volume [m^3] (d) Emission load (e) Tracing load

Figure A.4: Contour plots of scalar fields for `aachenBomb`

Table A.3: Correlation coefficient data for `FlameCube`

Relation Variables	Correlation Coefficient
Emission Load - Optical Thickness	0.1286
Emission Load - kPlanck	0.2105
Emission Load - Temperature	0.6481
Emission Load - Volume	-0.4565
Tracing Load - Optical Thickness	0.1257
Tracing Load - kPlanck	0.1225
Tracing Load - Temperature	0.3330
Tracing Load - Volume	-0.1035
Tracing Load - Emission Load	0.7310

Table A.4: Correlation coefficient data for `aachenBomb`

Relation Variables	Correlation Coefficient
Emission Load - Optical Thickness	0.4331
Emission Load - kPlanck	0.4331
Emission Load - Temperature	0.7946
Emission Load - Volume	N/A
Tracing Load - Optical Thickness	0.4937
Tracing Load - kPlanck	0.4937
Tracing Load - Temperature	0.7390
Tracing Load - Volume	N/A
Tracing Load - Emission Load	0.9380

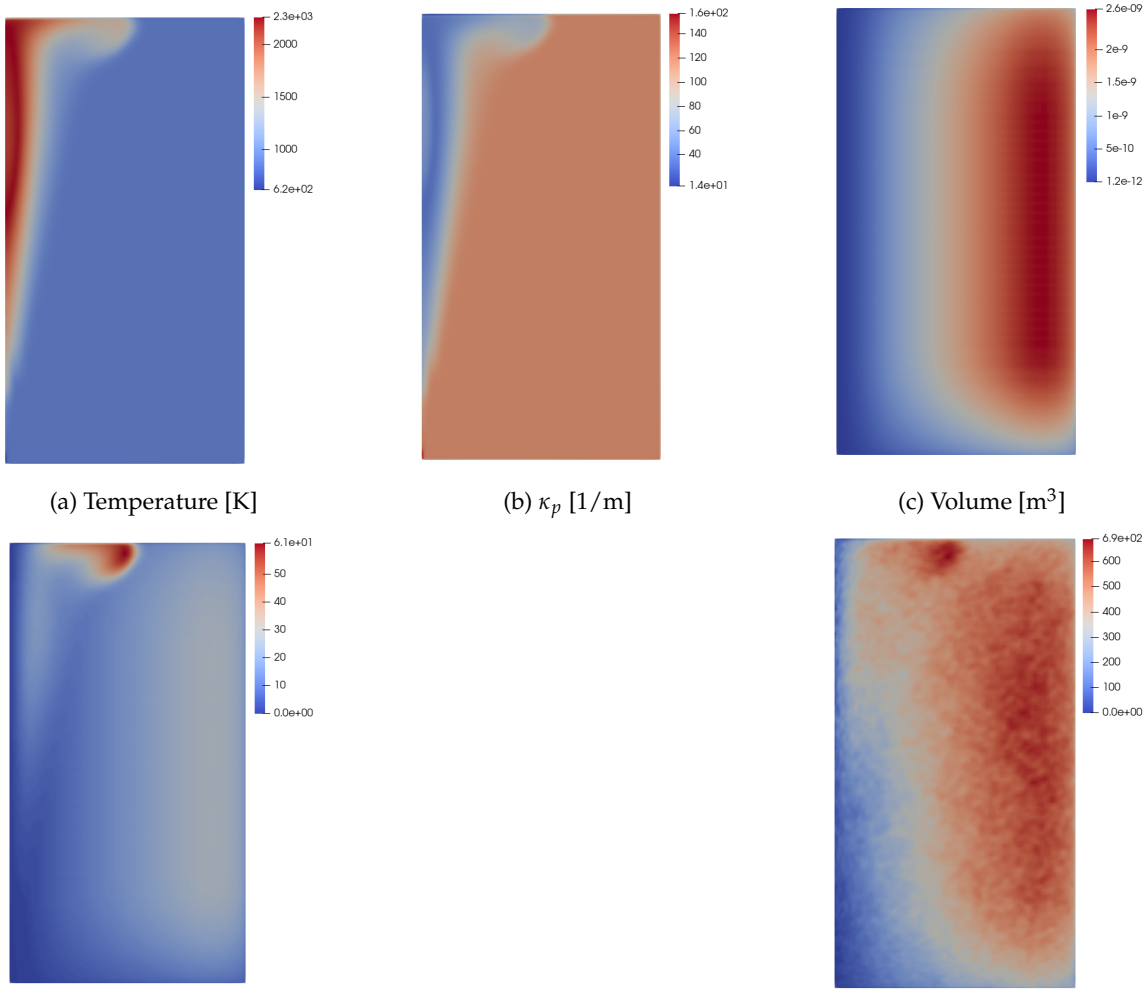

(a) Temperature [K]

(b) κ_p [1/m]

(c) Volume [m^3]

(d) Emission load

(e) Tracing load

Figure A.5: Contour plots of scalar fields for `sprayA`

Table A.5: Correlation coefficient data for `sprayA`

Relation Variables	Correlation Coefficient
Emission Load - Optical Thickness	0.3937
Emission Load - kPlanck	0.1108
Emission Load - Temperature	-0.1219
Emission Load - Volume	0.4906
Tracing Load - Optical Thickness	0.4549
Tracing Load - kPlanck	0.2031
Tracing Load - Temperature	-0.2042
Tracing Load - Volume	0.5082
Tracing Load - Emission Load	0.9478

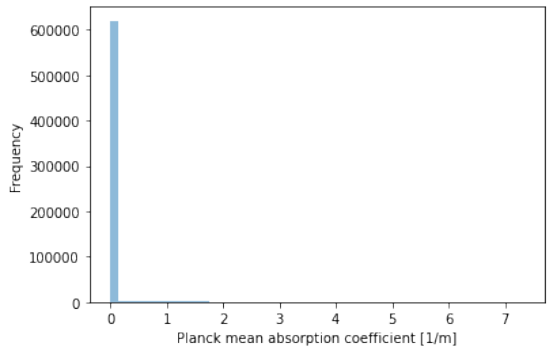

(a) Histogram for Planck mean absorption coefficient values for `smallPoolfire3D`

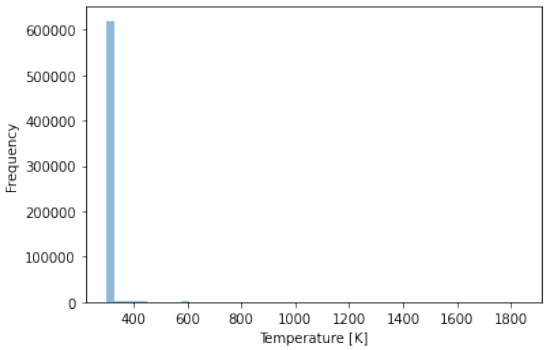

(b) Histogram for temperature values for `smallPoolfire3D`

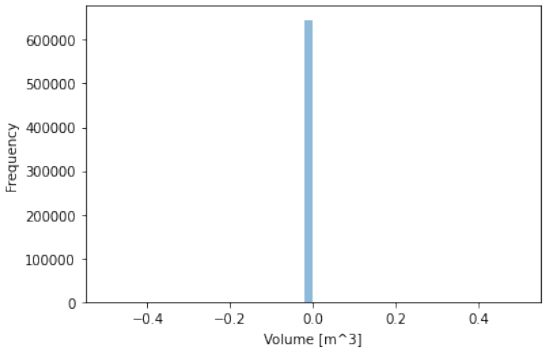

(c) Histogram for volume values for `smallPoolfire3D`

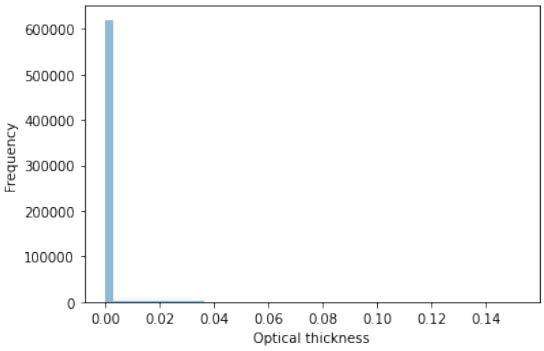

(d) Histogram for optical thickness values for `smallPoolfire3D`

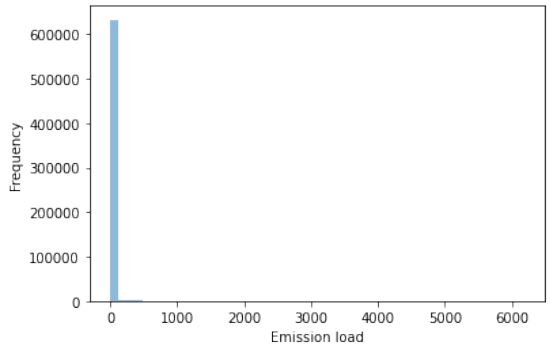

(e) Histogram for emission load values for `smallPoolfire3D`

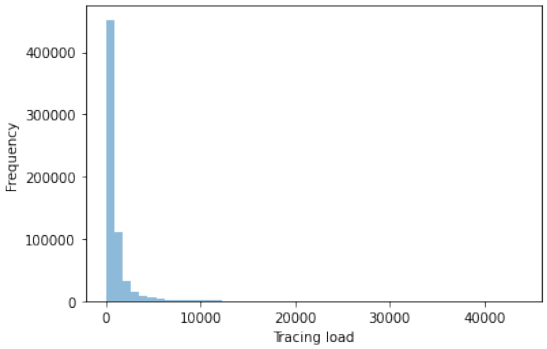

(f) Histogram for tracing load values for `smallPoolfire3D`

Figure A.6: Histograms for `smallPoolfire3D` data set

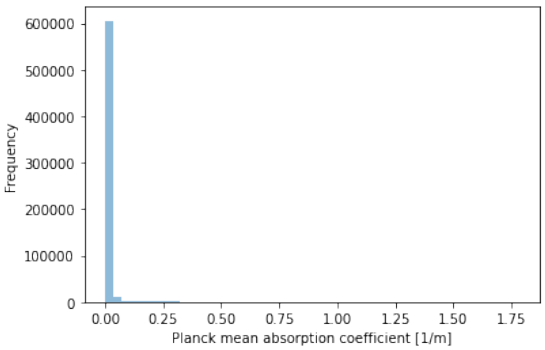

(a) Histogram for Planck mean absorption coefficient values for `smallPoolfire`

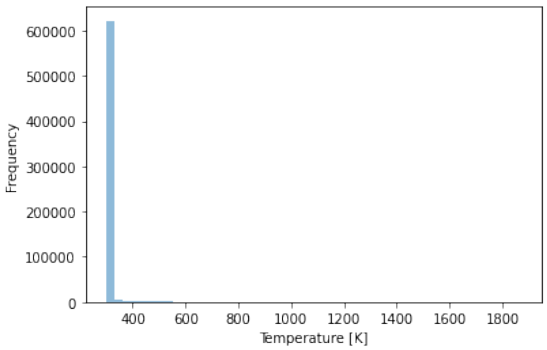

(b) Histogram for temperature values for `smallPoolfire`

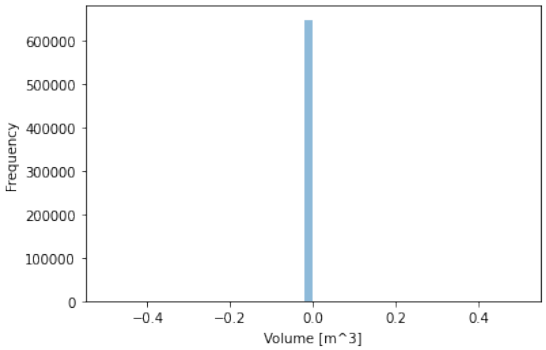

(c) Histogram for volume values for `smallPoolfire`

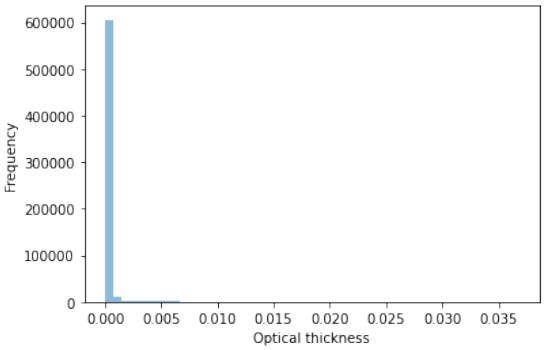

(d) Histogram for optical thickness values for `smallPoolfire`

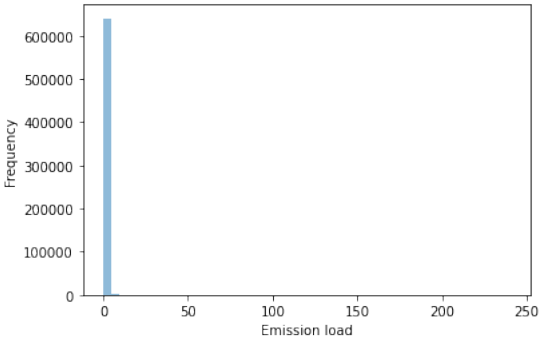

(e) Histogram for emission load values for `smallPoolfire`

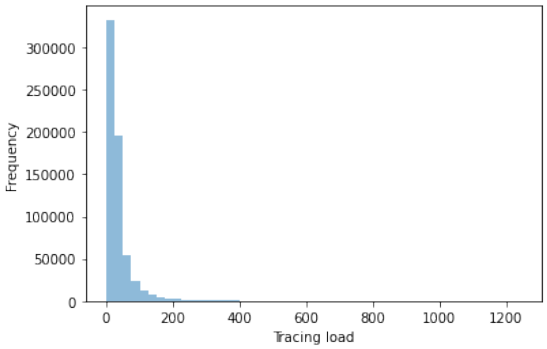

(f) Histogram for tracing load values for `smallPoolfire`

Figure A.7: Histograms for `smallPoolfire` data set

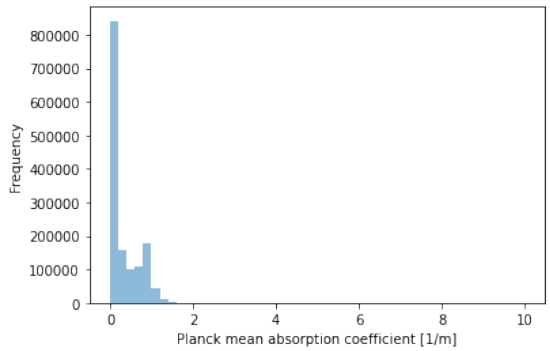

(a) Histogram for Planck mean absorption coefficient values for `FlameCube`

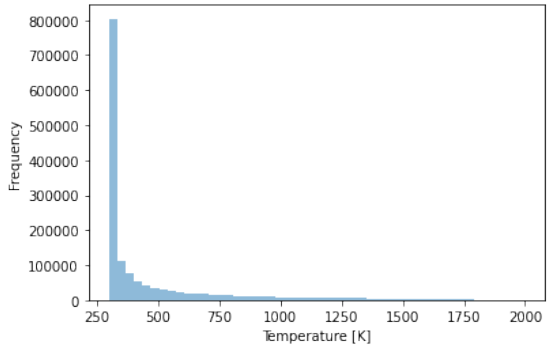

(b) Histogram for temperature values for `FlameCube`

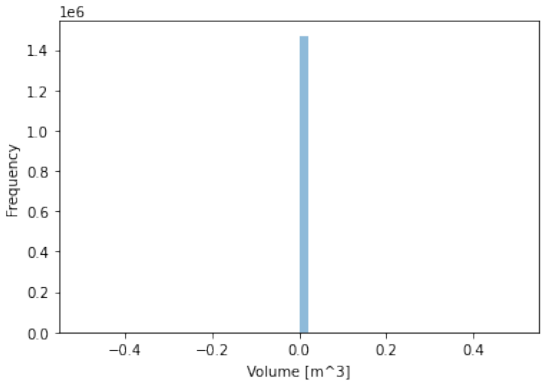

(c) Histogram for volume values for `FlameCube`

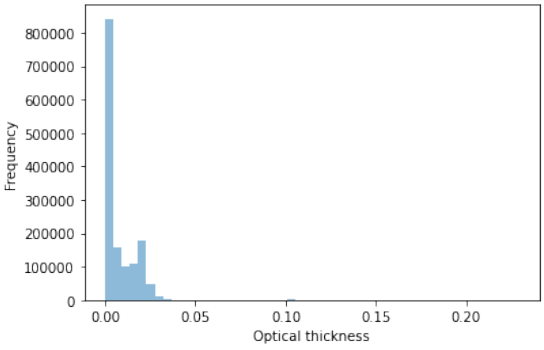

(d) Histogram for optical thickness values for `FlameCube`

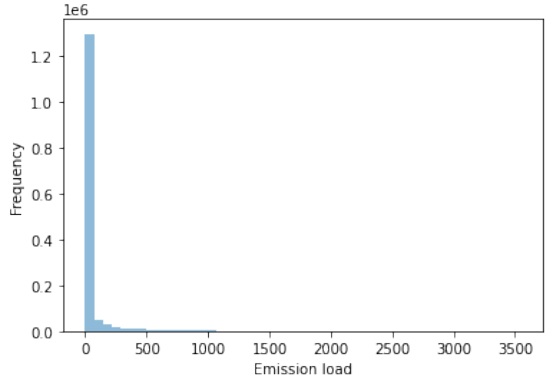

(e) Histogram for emission load values for `FlameCube`

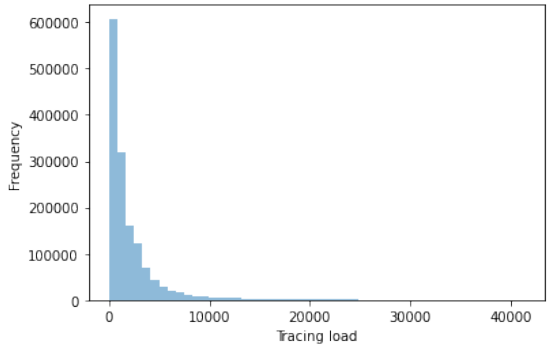

(f) Histogram for tracing load values for `FlameCube`

Figure A.8: Histograms for `FlameCube` data set

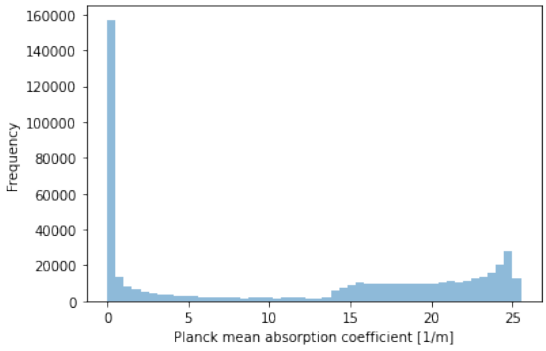

(a) Histogram for Planck mean absorption coefficient values for `aachenBomb`

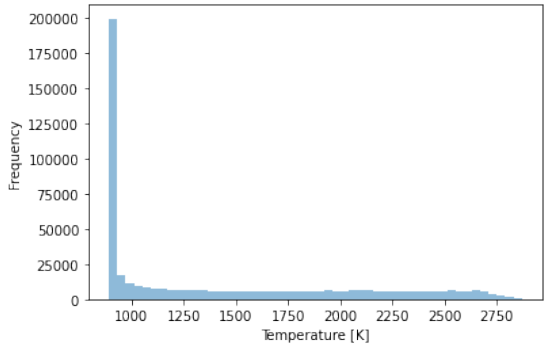

(b) Histogram for temperature values for `aachenBomb`

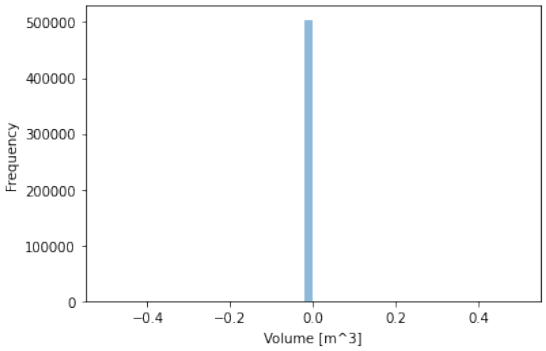

(c) Histogram for volume values for `aachenBomb`

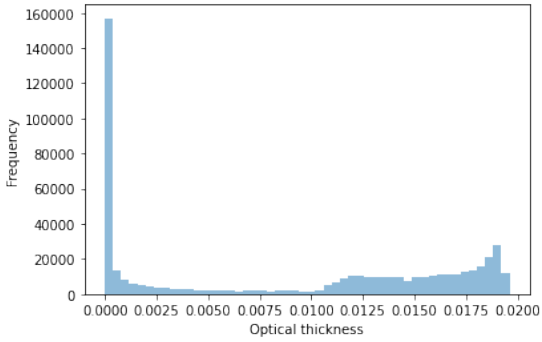

(d) Histogram for optical thickness values for `aachenBomb`

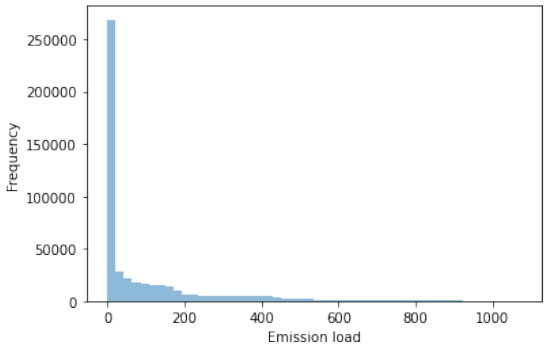

(e) Histogram for emission load values for `aachenBomb`

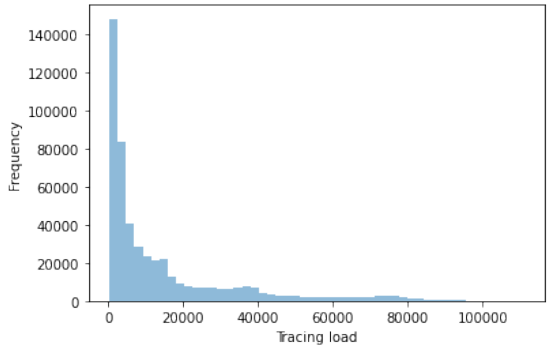

(f) Histogram for tracing load values for `aachenBomb`

Figure A.9: Histograms for `aachenBomb` data set

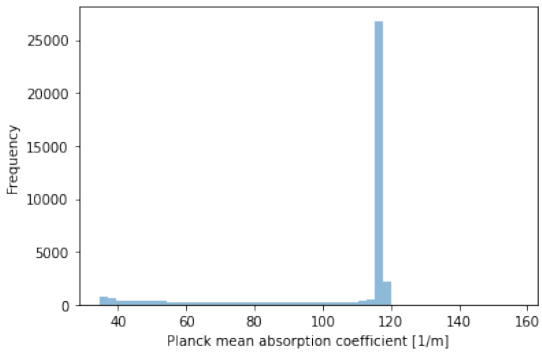

(a) Histogram for Planck mean absorption coefficient values for `sprayA`

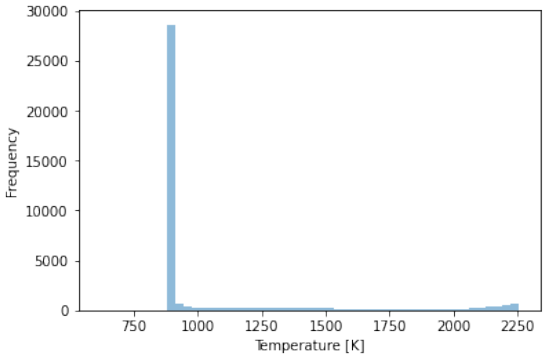

(b) Histogram for temperature values for `sprayA`

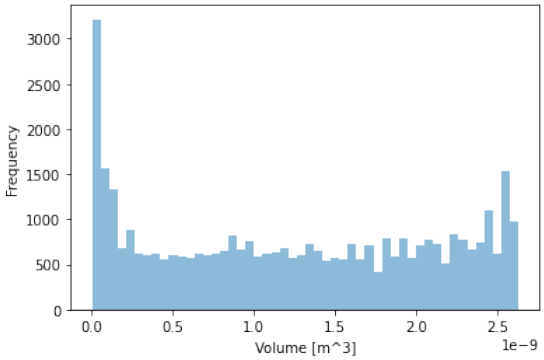

(c) Histogram for volume values for `sprayA`

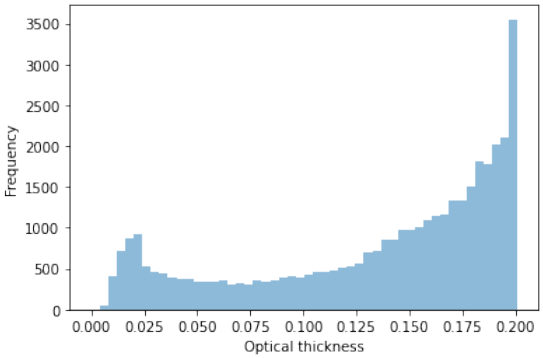

(d) Histogram for optical thickness values for `sprayA`

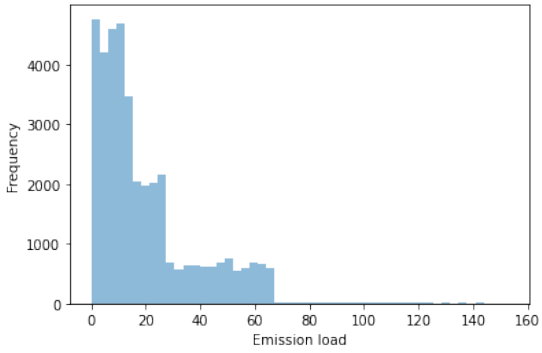

(e) Histogram for emission load values for `sprayA`

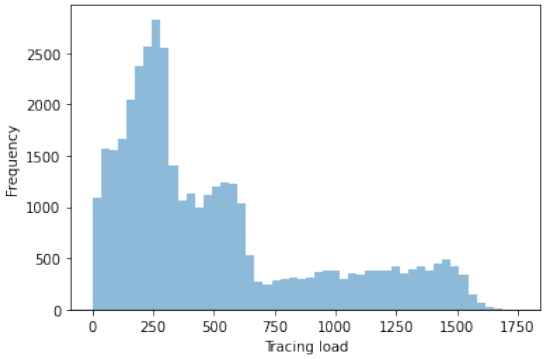

(f) Histogram for tracing load values for `sprayA`

Figure A.10: Histograms for `sprayA` data set